Structure of the human CTF18 clamp loader bound to PCNA

Giuseppina R. Briola[1¶], Muhammad Tehseen[1¶], Amani Al-Amodi[1], Phong Quoc Nguyen[1], Christos G. Savva[1], Samir M. Hamdan[1*] and Alfredo De Biasio[1*]

[1]Bioscience Program, Division of Biological and Environmental Sciences and Engineering, King Abdullah University of Science and Technology, Thuwal 23955, Saudi Arabia.

*Corresponding authors

E-mail: samir.hamdan@kaust.edu.sa or alfredo.debiasio@kaust.edu.sa

[¶]These authors contributed equally to this work.

Abstract

Sliding clamps like PCNA are crucial processivity factors for replicative polymerases, requiring specific clamp loaders for loading onto DNA. The human alternative clamp loader CTF18 interacts with the leading strand polymerase Pol ε and loads PCNA onto primer/template DNA using its RFC pentameric module. Here, we provide a structural characterization of the human CTF18 complex and its interaction with PCNA. Our cryo-EM data support that the Ctf8 and Dcc1 subunits of CTF18, which form the regulatory module interacting with Pol ε, are flexibly tethered to the RFC module. A 2.9 Å cryo-EM structure shows the RFC module bound to PCNA in an auto-inhibited conformation

similar to the canonical RFC loader, marking the initial step of the clamp-loading reaction. The unique RFC1 (Ctf18) large subunit of CTF18, which shows high relative mobility, is anchored to PCNA through an atypical low-affinity PIP box in the AAA+ domain and engages the RFC5 subunit using a novel β-hairpin at the disordered N-terminus. We show that deletion of this β-hairpin impairs the CTF18–PCNA complex stability and decreases the rate of primer synthesis by Pol ε. Our research identifies distinctive structural characteristics of the human CTF18-RFC complex, providing insights into its role in PCNA loading and the stimulation of leading strand synthesis by Pol ε.

Introduction

High fidelity and efficiency are critical for chromosomal DNA duplication in eukaryotes. This precision is achieved through the coordinated action of replicative DNA polymerases, Pol δ and Pol ε, anchored to the sliding clamp, and Proliferating Cell Nuclear Antigen (PCNA) (1). The ring-shaped PCNA homotrimer encircles DNA, enhancing the processivity of these polymerases in DNA replication and repair processes, including excision repair and homologous recombination (2), and plays an important role in sister chromatid cohesion establishment (3). The closed-ring topology of PCNA necessitates the transient opening of one interface to facilitate the incorporation and trapping of primer-template DNA. This critical function is executed by pentameric AAA+ ATPases, collectively known as clamp loaders (4-6). Extensive structural and biochemical work in different organisms (7-12) established a common mechanism for the clamp-loading reaction, which proceeds through three main steps

(13-18). Initially, the clamp loader engages with the intact clamp ring, adopting an autoinhibited configuration that precludes DNA binding (10). This stage sets the groundwork for the subsequent transition, where the clamp loader alters its conformation to an activated state. This change facilitates the opening of the clamp ring, creating a gap sufficiently large to permit the passage of duplex DNA and aligning the clamp loader for primer-template DNA interaction. The final phase of this process is initiated by the binding of DNA to the clamp loader, catalyzing ATP hydrolysis. This action prompts the closure of the clamp and the concurrent disassembly of the clamp loader, completing the cycle necessary for the engagement of the replicative polymerases to start DNA synthesis.

The canonical Replication Factor C (RFC), consisting of a large RFC1 subunit and four subunits (RFC2, RFC3, RFC4, and RFC5), acts as the primary clamp loader for PCNA (4, 19). However, eukaryotes also employ alternative loaders (20), including CTF18 (6, 21-24), highlighting the specificity of loading mechanisms facilitating DNA replication fidelity and efficiency.

Genome-wide analyses revealed that CTF18 predominantly facilitates PCNA loading on the leading strand, in contrast to the canonical RFC complex, which mainly loads PCNA on the lagging strand (25). Although CTF18 is not essential for bulk DNA replication in yeast (26, 27), it plays a vital role in ensuring sister chromatid cohesion (21, 28, 29). This may be due to its selective loading of PCNA linked to EcoI acetyltransferase (3), which acetylates Smc3, preventing cohesin destabilization by WapI (30-32). Recruitment of CTF18 to the leading strand is also important for activation of the replication checkpoint (22, 24, 33, 34).

The CTF18 complex features two distinct modules with separate functions (23, 35, 36): a catalytic RFC module for PCNA loading, consisting of a large RFC1-like subunit (hereby referred to as Ctf18), alongside the four RFC2, RFC3, RFC4 and RFC5 subunits utilized by the canonical RFC complex, and a regulatory module, made up of the Ctf8 and Dcc1 subunits. These latter two subunits attach to the Ctf18 C-terminus, forming the Ctf18-1-8 module. A long linker predicted to be flexible connects these two segments. Structural and functional studies have demonstrated that the interaction between the Ctf18-1-8 module and the catalytic domain of Pol2 ($Pol2_{CAT}$), the principal subunit of Pol ε, directs CTF18 to replication forks and boosts its clamp loading efficiency (34, 37). This interaction situates the clamp loader close to the primer/template junction, facilitating PCNA loading (34). $Pol2_{CAT}$ is tethered to the remainder of Pol ε via an unstructured linker, making it an integral component of the CMGE (CMG-Pol ε) core replisome complex (38). It has been proposed that Pol ε utilizes both the CMG helicase and PCNA as processivity factors to facilitate normal replication rates (39, 40). Tethering by the CMG complex might allow Pol ε to dissociate from the 3′ end of the leading strand but stay at the replication fork until leading strand synthesis restarts. Given Pol ε relatively weak interaction with PCNA (41), it is possible that multiple PCNA loading events on the leading strand via CTF18 are necessary to achieve full Pol ε processivity.

Although the structure of the Ctf18-1-8 module in association with $Pol2_{CAT}$ has been elucidated (34, 37), the architecture of the CTF18-RFC module and its interaction with PCNA remain uncharacterized. To investigate the clamp loading mechanism employed by CTF18, we reconstituted the full human CTF18 complex with PCNA and

determined its structure using cryo-electron microscopy (cryo-EM). Our cryo-EM data supports the prediction that the Ctf18-1-8 and RFC modules are flexibly tethered. The analysis yielded high-resolution reconstructions of the entire CTF18-RFC module bound to a closed PCNA ring. Although the overall architecture mirrors the autoinhibited state observed in the canonical RFC loader in a complex with PCNA (10), distinctive features within CTF18 were identified. These distinctions may offer insights into the specialized functional roles CTF18 plays in DNA replication.

Results

Structure of the human CTF18-PCNA complex

We employed single-particle cryo-EM to determine the structure of human CTF18 bound to PCNA. To this purpose, the full CTF18 complex, including Ctf8 and Dcc1, was expressed in insect cells and purified to homogeneity (Fig S1). The purified complex includes all subunits as shown in the SDS-PAGE gel (Fig S1). With the aim of trapping CTF18 in different steps of the clamp loading reaction, the complex was vitrified in the presence of ATP, PCNA, and primer/template DNA but omitting the Mg^{2+} cofactor to halt hydrolysis, and then imaged by cryo-EM (Fig S2). Surprisingly, image processing yielded only a major 3D class, including the CTF18-RFC pentamer bound to a closed PCNA ring (Fig 1a-b, S2-3 Fig), with no evidence of DNA density. The Ctf18-1-8 module, which is connected to the RFC module by a 91 amino acid linker (Fig 1a), is not resolved in the map (Fig 1b), suggesting it is flexibly tethered to the RFC module. The map was refined to a global resolution of 2.9 Å (S2-3 Fig), which allowed the model

building of the five CTF18-RFC subunits as well as the PCNA homotrimer (Fig 1c). The final model refines to a map-to-model FSC of 3.0 Å at 0.5 threshold, with good refinement statistics (S1 Table).

The five CTF18-RFC subunits are positioned on top of the closed PCNA ring, which is planar and undistorted (Fig 1c). A structural comparison shows that the CTF18-RFC pentamer was trapped in an autoinhibited conformation analogous to that reported for the canonical human (h) and yeast (sc) RFC (8, 10), pertaining to the initial step of the clamp loading reaction, right before clamp opening (Fig 1d). In such conformation, the AAA+ domains form an overstwisted and asymmetric spiral that is incompatible with DNA binding (8, 10). The AAA+, collar, and A' domains of the Ctf18 subunit (Fig 2a) align with the homologous domains of hRFC1 (Fig 2b). As in the hRFC structure (10), the Ctf18 subunit interacts with RFC2, RFC3, and PCNA1. Three main deviations from the hRFC–PCNA structure are observed (10): a different tilt of the PCNA ring (Fig 1c-d), significant mobility of the large Ctf18 subunit (Fig 1b and S2 Fig) and, importantly, the presence of a β-hairpin engaged to the outer surface of the RFC5 subunit, which we mapped to the disordered N-terminus of the Ctf18 subunit (Fig 2a and 2c). These features are analyzed in detail below.

Structure of the large subunit of CTF18

The Ctf18 subunit presents 22% identity with the homologous subunit RFC1 of hRFC and an overall structural conservation, with some deviations particularly in the A' domain (Fig 2b). Compared to the other subunits, the AAA+ domain of Ctf18 shows increased flexibility, as evidenced by the local resolution map of the complex (S2d Fig). Increased

flexibility was not detected in the RFC1 subunit of human RFC bound to PCNA (10). This discrepancy could be explained by the diminished interactions between Ctf18 and the adjacent RFC2 subunit, in contrast to the stronger interactions between RFC1 and RFC2 within the RFC complex. These differing interactions result in varying buried surface areas, with CTF18 and RFC having 1400 $Å^2$ and 2300 $Å^2$, respectively. Additionally, as explained below, the interaction between Ctf18 and PCNA is weaker compared to the interaction between RFC1 and PCNA, further contributing to these structural differences. The Ctf18 C-terminal region (residues 953-975) predicted to interact with the Ctf8 and Dcc1 subunits (Fig 2a) is invisible in the map.

The most striking feature is a small β-hairpin-containing fold mapped between residues 165-194 in the disordered N-terminus (Fig 2a and 2c) of the Ctf18 subunit, ~80 Å apart from the Ctf18 AAA+ domain, to which it is connected by a disordered linker of 86 amino acids (residues 195-280). This N-terminal fold plugs into a groove at the outer surface of the collar domain of the RFC5 subunit defined by helices α1, α3, α4, and α5 (Fig 3a). The resolution of the map in this region is sufficient for confident model building of the interface (Fig 3b). The interface buries 984 $Å^2$ and is characterized by both apolar and polar interactions (Fig 3a). A set of hydrophobic side chains protruding from Ctf18 β-hairpin (V178, V180, L190, L192) approaches a complementary patch of hydrophobic residues on RFC5 (L255 in α1; F287, V291 and F293 in α3; I336 and V337 in α5). The interface is further strengthened by several hydrogen bonds mostly mediated by main-chain atoms in the Ctf18 β-hairpin, and by a salt bridge between R193 of the Ctf18 β-hairpin and D292 of RFC5. It is worth highlighting that RFC2 separates the Ctf18 and RFC5 subunits. Despite this separation, Ctf18 projects the β-hairpin directly onto RFC5,

bypassing any interactions with RFC2 (Fig 2c). This observation supports that the β-hairpin functions as a “latch” to stabilize the CTF18-RFC structure.

Similarly to human CTF18, long regions predicted to be disordered by AlphaFold (42) are present in the N-terminal sequence of Ctf18 of lower eukaryotes. The β-hairpin region of human Ctf18 does not show strict sequence conservation, but a similar fold in the N-terminus of lower eukaryotes Ctf18 is predicted (Fig 2a). Therefore, lower eukaryotes may use a similar β-hairpin motif to bind the corresponding RFC5 subunit of the RFC-module complex, emphasizing its importance.

Interactions of CTF18 with PCNA

CTF18 engages two of the three PCNA protomers through four contact points involving the AAA+ domains of Ctf18, RFC2, RFC4, and RFC5 (Fig 1c and Fig 3c-d). The interactions with Ctf18, RFC2, and RFC5 subunits are analogous to those reported in the hRFC–PCNA complex (10). However, while Ctf18 engages PCNA1 via a PIP-box interaction as hRFC1 (10), its atypical PIP motif lacking aromatic residues (Fig 2a and Fig 3d) results in a smaller buried surface area (782 vs 1009 $Å^2$). This low-affinity interaction may contribute to the relative flexibility of the AAA+ domain of Ctf18 observed in the complex (S2d Fig). RFC2 contacts the Interdomain Connecting Loop (IDCL) of PCNA1, while the RFC5 PIP-box docks into the hydrophobic pocket of PCNA2 (Figure 3d), as already observed in hRFC (10). Differently from the hRFC–PCNA complex, where RFC4 is detached from PCNA (10), in CTF18, this subunit interacts with the IDCL of PCNA2 similarly as RFC2 binds PCNA1 (Figure 3d). The RFC4–PCNA interaction, which was also observed in the structure of scRFC bound

to an open PCNA (11), brings PCNA closer to the CTF18-RFC module, explaining the different tilt of the PCNA ring compared to the hRFC–PCNA complex (Fig 1c and 1d). Given the structure of scRFC bound to open PCNA (11), where all five RFC subunits are bound to PCNA (Fig 3c), we predict that a conformational shift in CTF18–RFC, specifically bringing the fifth subunit (RFC3) to engage PCNA3, would be necessary to disrupt the interface between PCNA1 and PCNA3, thereby opening the clamp and aligning the CTF18 subunits for primer-template DNA interaction. The reason for the absence of such an active CTF18 conformation in our cryo-EM analysis remains uncertain. However, similar to observations with the hRFC–PCNA complex, where an open-clamp state was not reported (10), this could be attributed to the hydrophobic regions of the open clamp interacting with the water-air interface, potentially leading to protein denaturation during the vitrification process to prepare the cryo-EM grids.

Nucleotide binding to the AAA+ modules

The map is consistent with nucleotides in four of the five AAA+ domains of the CTF18 subunits (Fig 4a). ATP is bound to subunits Ctf18, RFC2, and RFC5, while ADP appears to engage RFC3, consistent with the structure hRFC–PCNA complex reconstituted with ATPγS (10). Density for the adenine ring of ATP in the Ctf18 subunit is poor, likely a consequence of the increased mobility of the AAA+ domain of this subunit (Fig 4a). Compared to the canonical RFC1, the Walker A motif of Ctf18 contains a lysine residue (L378) instead of a valine, but this substitution does not appear to affect its interaction with the ATP nucleotide (S4 Fig). Since RFC3 lacks critical catalytic residues and bears a substitution in the Walker A motif (S4 Fig) (10), the presence of ADP, rather than a

product of ATP hydrolysis, probably results from co-purification of the complex where ADP contaminants are present. In the human RFC complex, it has been previously shown that an intact nucleotide binding site in RFC3 has an important structural role in the complex assembly (43, 44). If this is the case for CTF18, it remains to be established, but it is likely that ADP binding to this subunit may play a stabilizing role in all RFC-like loaders.

Differently from the hRFC–PCNA complex, where RFC4 is bound to ATPγS, in CTF18, this subunit is not engaged with a nucleotide (Fig 4a). The residues in the AAA+ of RFC4 of CTF18 coordinated to ATPγS in hRFC are displaced and incompatible with nucleotide binding. Interestingly, mutation of the conserved K84 residue in the ATP-binding motif of RFC4 in hRFC did not impair the ability of this subunit to assemble with other RFC subunits (44). In agreement, our structure shows that the lack of ATP binding to RFC4 does not preclude the assembly of the CTF18-RFC pentamer in the autoinhibited conformation. However, considering the importance of ATP binding of RFC4 for the hRFC clamp loading function (43-45), it is expected that ATP binding to RFC4 in CTF18 is required to switch to an enzymatically active conformation.

The asymmetric spiral of the CTF18 AAA+ pentamer (Fig 4a-b) disrupts the active sites at the Ctf18/RFC2, RFC2/5, and RFC5/4 interfaces (Fig 4c). At these interfaces, the *trans*-acting arginine fingers are positioned too far away to interact with the γ-phosphate of ATP (*e.g.*, ~9 Å for Arg184 of RFC2, ~10 Å for Arg168 of RFC5, and ~7 Å for Arg193 of RFC4) (Fig 4c). Prior research has indicated that the Ctf18/RFC2 particular site is not essential for clamp loading by various loaders (46-48), while the others are critical for the clamp-loading activity of eukaryotic RFCs.

In CTF18, the AAA+ spiral is overtwisted in a manner reminiscent of the autoinhibited conformations observed in hRFC and scRFC (8, 10) (Fig 1d), leading to steric hindrance that impedes DNA binding (Fig 4b). Specifically, the overtwisted RFC3 and RFC4 subunits occupy the space normally filled by DNA. In the autoinhibited structure of hRFC, the β-hairpin (residues 68-88) located at the base of RFC3 also referred to as "E-plug", extends towards the anticipated location of DNA and interacts with the Rossmann fold of RFC1 (10). Conversely, in CTF18, while this same β-hairpin is oriented toward the interior of the DNA-binding channel (Fig 4d), it does not make direct contact with the Ctf18 subunit. Collectively, the E-plug appears a conserved feature in eukaryotic clamp loaders, underlying its importance in maintaining the pentamer in its autoinhibited conformation, by preventing DNA access through the central channel. We observed that human CTF18 shares an additional conserved feature with the yeast RFC, specifically the presence of a separation pin in the CTF18 large subunit. This pin is analogous to the one that interacts with DNA in the yeast RFC complex (Fig 4e) [11].

To discount the possibility that the absence of the Mg^{2+} ions in the cryo-EM sample could have hindered the proper assembly of the CTF18 pentamer for DNA engagement, we used cryo-EM to visualize CTF18 with PCNA, primer-template DNA, ATP, and Mg^{2+} (S5 Fig, S1 Table). Despite the inclusion of Mg^{2+}, the resulting 3.2 Å reconstruction of the complex remained in a configuration analogous to that without Mg^{2+} (Fig 5a-b, S6 Fig). In this reconstruction, distinct density for Mg^{2+} is noted in the active sites of RFC2 and RFC5, coordinating ATP (Fig 5b). Similar to the map without Mg^{2+}, ADP coordination is present in RFC3, while RFC4 is not engaged with any

nucleotide. These findings collectively imply that the presence of Mg^{2+} in the nucleotide binding sites does not influence the transition of CTF18 from an autoinhibited to an active state. This result also confirms the remarkable stability of the autoinhibited conformation, even in hydrolyzing conditions.

The Ctf18 β-hairpin plays a role in stimulating DNA synthesis by Pol ε

Based on the structures reported herein, the β-hairpin at the disordered N-terminal domain of Ctf18 is a distinctive feature that may serve to stabilize the CTF18-RFC pentamer and maximize its clamp loading efficiency. To investigate the functional importance of the β-hairpin, we purified a CTF18 mutant with a truncation at the disordered N-terminal domain of the Ctf18 subunit, specifically, the segment spanning residues 165-194 (CTF18-RFC$^{\Delta 165\text{-}194}$). This mutation eliminates the entire Ctf18 β-hairpin and is expected to destabilize the CTF18-RFC pentamer. In agreement, when mutant CTF18 was imaged by cryo-EM with PCNA in the same conditions used for wild type CTF18, only a small subset of particles of the complex was observed, while the majority of particles contained dissociated PCNA (S7 and S8 Fig). We hypothesized that this destabilizing mutation in CTF18 may reduce its efficiency in loading PCNA onto DNA, thereby resulting in diminished stimulation of primer synthesis by Pol ε.

To test this hypothesis, we performed primer extension assays using Pol ε, PCNA, and either wild-type or mutant CTF18 constructs to assess their ability to stimulate DNA synthesis by Pol ε. Our results indicate a significant reduction in primer extension products when the β-hairpin was deleted (Fig 6a). Measurement of band

intensities revealed an approximately two-fold decrease in the amount of extended primer produced by the mutant compared to the wild-type (Fig 6b). To further support that the observed effect on primer extension is due to the mutation, we conducted a concentration titration comparing wild-type and mutant CTF18 (S9 Fig). The CTF18 mutant displayed altered concentration dependencies compared to the wild-type, thereby validating the mutant phenotype and underscoring the structural importance of the β-hairpin feature.

Discussion

In this work, we reported the structure of the human CTF18 clamp loader bound to PCNA in the presence of ATP with or without Mg^{2+} ions. Our cryo-EM data, together with previous work (34, 37), support that the Ctf8 and Dcc1 subunits of CTF18, forming the regulatory module interacting with Pol ε (37), are flexibly tethered to the RFC-module via binding to the Ctf18 C-terminus, which is separated by the N-terminal RFC1-like module of Ctf18 by ~90 amino acid flexible linker. Therefore, CTF18 comprises two structurally distinct modules that cooperate to load PCNA onto the leading strand, facilitating replication by Pol ε.

The CTF18-PCNA complex was observed in an autoinhibited conformation, which prevents DNA binding. This mirrors the similar conformation in hRFC and scRFC, as previously reported (10, 11). Such conformation represents a transient encounter complex that occurs early in the clamp loading process, before the opening of the clamp. Despite the variations in the large RFC subunit in the two assemblies, we demonstrate a striking architectural conservation between the alternative human clamp

loader CTF18 and the canonical RFC. Specifically, CTF18 utilizes three subunits (Ctf18, RFC2, RFC5, and RFC4) to engage two PCNA protomers. However, the engagement of the third PCNA protomer by RFC3 is necessary to initiate the opening of the PCNA ring interface, a process that requires a conformational shift of the AAA+ pentamer from an autoinhibited to an active state. Supporting this, previous structural studies on scRFC have shown that the conformation of RFC bound to open PCNA is facilitated through a 'crab-claw' mechanism, which is inherently predisposed to DNA binding (11). This conformational change creates an opening between the A′ segment and the AAA+ module in the A subunit, allowing primer-template DNA to bind within the RFC inner chamber (11) (Fig 4C). Remarkably, this significant conformational shift occurs rapidly (49), does not depend on ATP hydrolysis, and ensures the sequential binding of PCNA and the DNA substrate in the correct order. While our study did not resolve the active conformation of CTF18, the observed structural conservation in the autoinhibited state, particularly of the large Ctf18 subunit (Fig 2), suggests that a similar 'crab-claw' mechanism may facilitate the transition of CTF18 to its active state for PCNA opening and DNA binding. While our work was being finalized, several cryo-EM structures of human CTF18 bound to PCNA and primer/template DNA were reported by another group (50). These findings confirm the distinct features of CTF18 observed in our structures and validate our predictions regarding the significant similarities between CTF18-RFC and canonical RFC in loading PCNA onto a ss/dsDNA junction.

The main structural differences between CTF18 and the canonical RFC include increased mobility of the large subunit and the presence of a β-hairpin that attaches to the RFC5 subunit. The mobility of the large subunit is likely enhanced by the low-affinity

PIP motif that anchors it to the PCNA ring. We propose that the β-hairpin may have evolved to counterbalance the mobility of the large subunit, helping to maintain its connection to the RFC pentamer and stabilizing the clamp loader structure. Our structural data and functional assays indeed show that deletion of the β-hairpin results in reduced stability of the CTF18–PCNA complex and diminished activity of CTF18 in stimulating Pol ε primer synthesis, likely by reducing CTF18 efficiency in PCNA loading (Fig 7). Interestingly, a recent work reporting cryo-EM structures of the yeast homolog of CTF18 bound to PCNA (51) does not support the presence of a stable β-hairpin at the N-terminus of the Ctf18 subunit engaged to the collar of the Rfc3 subunit. Therefore, the functional β-hairpin we observed in human CTF18 appears a distinct feature that pertains to higher eukaryotes, required to maximize the activity of CTF18 in loading PCNA onto the leading strand.

Materials and Methods

Protein expression and purification

Preparation of CTF18-RFC

MultiBac™ expression system (Geneva Biotech) was used to express human Ctf18-RFC2-5 along with two additional cohesion-specific factors, Dcc1 and Ctf8 (named hereafter CTF18-RFC) in Sf9 insect cells. For this purpose, insect cells optimized sequences of N-terminus twin Strept-tagged TEV Ctf18, RFC2, and RFC4 were cloned in pACEBac1 plasmid with independent promoters and terminators, and N-terminus 6X histidine-tagged RFC3, RFC5, Dcc1 and Ctf8 were cloned in pIDS plasmid with

independent promoters and terminators by GenScript. Finally, the single transfer vector with different subunit assemblies was generated using *cre* recombinase according to the MultiBac™ expression system user manual. CTF18-RFC encoding all seven subunits in a single MultiBac™ expression plasmid (pACEBac1) was transformed into DH10MultiBac™ cells to make bacmid DNA. To prepare the baculovirus, bacmid DNA containing all subunits was transfected into Sf9 cells using FuGENE® HD (Promega) according to the manufacturer's instructions. This baculovirus prep was amplified twice to obtain a higher titer virus (P3 virus). The expression of CTF18-RFC then proceeded by transfecting a 6 L Hi5 suspension culture at a density of 2×10^6 cells/mL with the P3 virus for 60-65 hours.

Cells were collected by centrifugation at 5,500 xg for 10 minutes and re-suspended in lysis buffer [50 mM Tris-HCl (pH 7.5), 300 mM NaCl, 20 mM imidazole, 5 mM BME, 0.1% Nonidet P-40, 10% glycerol and one EDTA-free protease inhibitor cocktail tablet/50 mL]. All further steps were performed at 4° C. Cells were sonicated and debris was removed by centrifugation at 95,834 xg for 1 hour at 4 °C. The resultant supernatant was directly loaded onto a HisTrap HP 5 mL affinity column (Cytiva) pre-equilibrated with buffer A [50 mM Tris-HCl (pH 7.5), 300 mM NaCl, 20 mM imidazole, 5 mM BME and 10% glycerol]. After loading, the column was washed with 50 mL of buffer A and the bound fractions were eluted by gradient with 50 mL of buffer B [50 mM Tris-HCl (pH 7.5), 300 mM NaCl, 500 mM imidazole, 5 mM BME, and 10% glycerol]. The eluents were pooled and directly loaded onto Strept Trap XT 1 mL affinity column pre-equilibrated with buffer A [50 mM Tris-HCl (pH 7.5), 300 mM NaCl, 5 mM BME and 10% glycerol]. After loading, the column was washed with 10 mL of buffer A, followed by step

elution with buffer B [50 mM Tris-HCl (pH 7.5), 300 mM NaCl, 50 mM Biotin, 5 mM BME, and 10% glycerol]. Eluents were pooled and incubated with the TEV protease overnight. Fractions were concentrated to 1 mL and loaded onto HiLoad 16/600 Superdex 200 pg pre-equilibrated with gel filtration buffer [50 mM Tris-HCl (pH 7.5), 200 mM NaCl, 1 mM DTT, and 10% glycerol]. Protein fractions were pooled in a total volume of 1.6 mL, flash frozen, and stored at -80°C.

Preparation of PCNA

To express PCNA BL21(DE3) *E. coli* cells were transformed with WT PCNA plasmid. The transformed cells were grown at 37°C in 2YT media supplemented with ampicillin to an OD600 of 1.2. The cell cultures were induced with 0.5 mM isopropyl-beta-D-1-thiogalactopyranoside (IPTG) and let them grow for 19 hours at 16°C. Cells were then harvested by centrifugation at 5500 xg for 10 minutes and then re-suspended in lysis buffer [50 mM Tris-HCl (pH 7.5), 750 mM NaCl, 20 mM imidazole, 5 mM BME, 0.2% Nonidet P-40, 1 mM PMSF, 5% glycerol and one EDTA-free protease inhibitor cocktail tablet/50 mL]. The cells were lysed with 2 mg/mL of lysozyme at 4°C for 30 minutes. Cells were sonicated and debris was removed by centrifugation at 22,040 xg for 20 minutes at 4°C. The cleared cell lysate was directly loaded onto a HisTrap HP 5 mL affinity column (Cytiva) pre-equilibrated with buffer A [50 mM Tris-HCl (pH 7.5), 500 mM NaCl, 20 mM imidazole, 5 mM BME and 5% glycerol]. The column was firstly washed with 50 mL of buffer A and then with 50 mL of buffer B containing low salt [50 mM Tris-HCl (pH 7.5), 100 mM NaCl, 500 mM imidazole, 5 mM BME, and 5% glycerol]. The eluents were pooled and directly loaded onto HiTrap Q HP 5 mL anion exchange column (GE Healthcare) pre-equilibrated with buffer D [50 mM Tris-HCl (pH 7.5), 100

mM NaCl, 5 mM BME and 5% glycerol]. The column was washed with 50 mL of buffer D after loading, followed by elution of 50 mL gradient with buffer E [50 mM Tris-HCl (pH 7.5), 1 M NaCl, 5 mM BME, and 5% glycerol]. Eluents were pooled and concentrated to 1.5 mL and loaded onto HiLoad 16/600 Superdex 200 pg pre-equilibrated with gel filtration buffer [50 mM Tris-HCl (pH 7.5), 150 mM NaCl, 1 mM DTT, and 5% glycerol]. Protein fractions were pooled, flash-frozen, and stored at -80 °C.

Preparation of polymerase ε

MultiBac™ expression system (Geneva Biotech) was used to express human DNA Pol ε in Sf9 insect cells. For this purpose, insect cells optimized sequence of the catalytic subunit, p261 was cloned in pACEBac1 and p59, C-terminus TEV twin Strept-tagged p17, and N-terminus 8X histidine-tagged TEV p12 along with independent promoters and terminators were cloned in pIDS by the GenScript. Finally, the single transfer vector with different subunit assemblies was generated using *cre* recombinase according to MultiBac™ expression system user manual. To prepare the baculovirus, the bacmid DNA of Pol ε was transfected into Sf9 cells using FuGENE® HD (Promega) according to the manufacturer's instructions. The resulting supernatant was obtained as the P1 virus stock which was then amplified to obtain P2 virus stock. P2 virus stock was then further amplified to obtain P3 virus stock for large-scale expression. Pol ε was expressed by transfecting 4 L of Sf9 suspension culture at 2×10^6 cells/mL density with P3 virus. Cells were harvested after 72 hours by centrifugation at 5,500 xg for 10 minutes and re-suspended in 200 mL of lysis buffer [50 mM HEPES (pH 8), 20 mM Imidazole, 400 mM NaCl, 5 mM β-Mercaptoethanol, 5% (v/v) Glycerol, 0.1% NP-40, 1 mM PMSF and EDTA-free protease inhibitor cocktail tablet/50 mL (Roche, UK)]. Cells were sonicated

and debris was removed by centrifugation at 95,834 xg for 1 hour at 4 °C. The resultant supernatant was directly loaded onto a HisTrap HP 5 mL affinity column (Cytiva) equilibrated with buffer A [50 mM HEPES (pH 8), 20 mM Imidazole, 400 mM NaCl, 5mM β-Mercaptoethanol, 5% (v/v) Glycerol and EDTA-free protease inhibitor cocktail tablet/50 mL (Roche, UK]. After loading, the column was washed with 50 mL of buffer A and the bound fractions were eluted by gradient with 50 mL of buffer B [50 mM HEPES (pH 8), 500 mM Imidazole, 300 mM NaCl, 5 mM β-Mercaptoethanol, 5% (v/v) Glycerol and EDTA-free protease inhibitor cocktail tablet/50 ml (Roche, UK)]. Peak fractions containing Pol ε subunits were pooled and loaded directly onto Strep Trap XT 5 mL (Cytiva) column equilibrated with buffer C [50 mM HEPES (pH 8), 250 mM NaCl, 5 mM β-Mercaptoethanol, 5% (v/v) Glycerol] and EDTA-free protease inhibitor cocktail tablet/50 mL (Roche, UK)]. After loading, the column was washed with 50 mL of buffer C and the bound fractions were incubated for 2-4 hours with 15 mL of 100% buffer D [50 mM HEPES (pH 8), 100 mM NaCl, 50 mM Biotin, 5 mM β-Mercaptoethanol, 5% (v/v) Glycerol] and EDTA-free protease inhibitor cocktail tablet/50 mL (Roche, UK)] and eluted further with 30 mL of 100% buffer D. Fractions that contain all Pol ε subunits were pooled and incubated with the TEV protease for overnight and loaded onto an anion exchanger, Mono Q 5/50 GL column (Cytiva) pre-equilibrated with buffer E [50 mM HEPES (pH 8), 100 mM NaCl, 5 mM β-Mercaptoethanol and 5% Glycerol]. After loading, the column was washed with 15 mL of buffer E. The Pol ε was eluted with a 10 mL gradient from 100 mM NaCl to 1 M NaCl in 50 mM HEPES (pH 8), 5 mM β-Mercaptoethanol, and 5% Glycerol. The fractions that contained all Pol ε subunits were combined and concentrated to 1 mL and loaded onto HiLoad 16/600 Superdex 200 pg

(Cytiva) pre-equilibrated with gel filtration buffer [50mM HEPES (8), 200 mM NaCl, 1 mM DTT and 5% Glycerol]. Protein fractions were pooled, flash-frozen, and stored at −80°C.

All protein concentrations were calculated by measuring their absorbance at 280 nm using the extinction coefficients calculated from the amino acid composition (CTF18-RFC: 216,360 M^{-1} cm^{-1}; PCNA: 47,790 M^{-1} cm^{-1}, Pol ε: 351,470 M^{-1} cm^{-1}).

DNA substrates

For the primer/template substrates used in all the structures described here, 80 base pairs template strand 5'-TTTTTTTTTTTTTTTTTTTTTTTTTTTTTTTTTTTTTTTTGACTGCAC GAATTAAGCAATTCGTAATCATGG TCATAGCT-3' was annealed to a 39 base pairs primer containing a 3' dideoxy cytosine chain terminator 5'-AGCTATG ACCATGATTACGAATTGCTTAATTCGTGCAGT[ddC]-3' to form the P/T substrate. The strands were mixed in an equimolar ratio in the presence of 20 mM Tris pH 7.5 and 25 mM NaCl. The annealing reaction was performed by incubating the P/T at 92°C for 2 minutes followed by slow cooling to room temperature overnight. All oligonucleotides were purchased from IDT Integrated DNA Technologies.

Primer extension assay

The primer extension reaction was conducted in a reaction buffer containing [40 mM HEPES (pH 7.6), 100 mM K-glutamate, 1 mM DTT, 10 mM Mg-Acetate, 200 µg/mL BSA, 1 mM ATP, 100 µM each of dATP, dTTP, and dGTP, 20 µM dCTP, and 10 µCi of

[^{32}P]-dCTP (Hartmann)]. Two nanomolar of the primed-M13 template were initially incubated at 37 °C for 10 minutes with 100 nM PCNA, 400 nM RPA, and either CTF18-RFC WT or CTF18-RFC$^{\Delta 165\text{-}194}$. The reaction was initiated by the addition of 30 nM Pol ε. Reactions were stopped at the indicated time point by adding 50 mM EDTA and electrophoresed on 0.7% alkaline agarose gel at 35 V for 17 hours. The gel was backed with DE81 paper, compressed, and imaged in a Sapphire Biomolecular Imager (Azure Biosystems). All the experiments were performed in triplicate.

Primer extension substrates

Oligo (592:TAACGCCAGGGTTTTCCCAGTCACG) (Integrated DNA Technologies) was annealed to 50 nM M13mp18 single-stranded DNA (New England Biolabs) in a reaction buffer consisting of [10 mM Tris-HCl (pH 7.6), 100 mM NaCl and 5 mM EDTA]. The mixture was heated to 95 °C for 5 minutes, then cooled gradually to room temperature. The unannealed oligonucleotide was removed using a QIAquick PCR purification kit (Qiagen).

Cryo-EM grids preparation and data collection

For all the complexes (WT and mutant), UltraAuFoil® R1.2/1.3 Au 300 grids were glow-discharged at 30 mA for 30 seconds on an EasyGlow glow-discharge unit. For the preparation of the complex without Mg^{2+} **(Dataset 1 and Dataset 3)**, P/T DNA, ATP, CTF18-RFC WT/CTF18-RFC$^{\Delta 165\text{-}194}$, and PCNA were mixed in order. The final concentrations were 5.6 μM P/T DNA, 0.2 mM ATP, 1.5 μM CTF18-RFC WT/CTF18-

RFC$^{\Delta 165\text{-}194}$, and 7.5 μM PCNA. The buffer this was performed in comprised 50 mM Tris-HCl pH 7.5, 200 mM NaCl, 1 mM DTT, and 0.5 mM ATP. 3 μL of the sample was applied to the grid, blotted for 2 s at blot force -5, and plunged frozen into liquid ethane using a Vitrobot Mark IV (FEI Thermo Fisher), which was set at 4°C and 100% humidity. For the preparation of CTF18-RFC /PCNA/P-T DNA/ATP/Mg^{2+}complex **(Dataset 2)**, the components P/T DNA, ATP, Mg^{2+}, CTF18-RFC, and PCNA were mixed in order. The final concentrations were 5.6 μM P/T DNA, 0.2 mM ATP, 1.9 mg/mL Mg^{2+}, 1.5 μM CTF18-RFC, and 7.5 μM PCNA. The buffer this was performed in comprised 50 mM Tris-HCl pH 7.5, 200 mM NaCl, 1 mM DTT, 0.5 mM ATP, and 5 mM Mg^{2+}. 3 μL of the sample was applied to the grid in the same way as above for data collection. Cryo-EM data for all the samples were collected on a Thermo Fisher Scientific Titan Krios G4 transmission electron microscope at KAUST. Electron micrographs for **Dataset 1** (CTF18-RFC-PCNA with ATP in the absence of Mg^{2+}), were collected using a Falcon 4i detector at a dose rate of 7.5 e^-/pix/sec for 5 seconds and a calibrated pixel size of 0.93 Å. Focusing was performed over a range between -2.7 μm and -1.5μm, in 0.3 μm intervals. Electron micrographs for **Dataset 2** (CTF18-RFC-PCNA with ATP and Mg^{2+}) were collected using a Falcon 4i detector at a dose rate of 8.02 e^-/pix/sec for 5 seconds and a calibrated pixel size of 0.93 Å. Focusing was performed over a range between -2.7 μm and -1.5 μm, in 0.3 μm intervals. Electron micrographs for **Dataset 3** (CTF18-RFC$^{\Delta 165\text{-}194}$-PCNA with ATP and in the absence of Mg^{2+}) were collected using a Falcon 4i detector at a dose rate of 7.4 e^-/pix/sec for 5 seconds and a calibrated pixel size of 0.93 Å. Focusing was performed over a range between -2.7 μm and -1.5 μm, in 0.3 μm intervals.

Cryo-EM image processing

Preprocessing of all datasets (**Dataset 1**: CTF18-RFC, ATP, primer/template DNA and PCNA; **Dataset 2:** CTF18-RFC, ATP, Mg^{2+}, primer/template DNA and PCNA; **Dataset 3**: CTF18-RFC$^{\Delta 165\text{-}194}$, ATP, primer/template DNA and PCNA) was performed as follows: the micrographs were corrected for beam-induced motion and then integrated using MotionCor2 (54). All frames were retained and a patch alignment of 4x4 was used. CTFFIND-4.12 estimated Contrast Transfer Function (CTF) parameters for each micrograph (53). Integrated movies were inspected with Relion-4.0 (**Dataset 1** and **Dataset 2**) and Relion-5.0 (**Dataset 3**) for further image processing (7906 movies for **Dataset 1**, 6181 movies for **Dataset 2**, and 6499 movies for **Dataset 3**) (54). Particle picking was performed in automated mode using Topaz (55) for **Dataset 1**. Particle extraction was carried out from micrographs using a box size of 55 pixels (pixel size: 3.65 Å/pixel). An initial dataset of 2 x 10^6 particles was cleaned by 2D classification followed by 3D classification with alignment. Three 3D classes were generated with populations of 31, 28, and 40%. 3D refinement, CtfRefine, and polishing were performed on the selected 3D classes corresponding to populations 31 and 40%. A bigger box size, 480 pixels (pixel size: 0.93 Å/pixel) was used to re-extract the particles. 3D refinement, CtfRefine, and polishing yielded reconstruction at 2.9 Å.

Particle picking was performed in reference-based mode for **Dataset 2**. Particle extraction was carried out from micrographs using a box size of 55 pixels (pixel size of 3.65 Å/pixel). An initial dataset of 3 x 10^6 particles was cleaned by 2D classification followed by 3D classification with alignment. Three 3D classes were generated with 30,

33, and 36% populations. 3D refinement, CtfRefine, and polishing were performed on the selected 3D classes corresponding to populations 33 and 36%. 3D refinement, CtfRefine, and polishing yielded reconstruction at 3.2 Å. Particle picking was performed in automated mode using Topaz (55) for **Dataset 3**. Particle extraction was done from micrographs using a box size of 220 pixels (pixel size: 0.93 Å/pixel). An initial dataset of 1 x 10^6 particles was cleaned by 2D classification.

Molecular Modelling

The structure of the Ctf18 large subunit of human CTF18 (Q8WVB6, residues 277-805) was generated with Phyre2 (56), using as a template the sequence of human RFC1 (P35251, residues 581-1034). The Ctf18 subunit model was then aligned to the RFC1 subunit in the structure of the human RFC clamp loader bound to PCNA in an autoinhibited conformation (PDB 6VVO, (10)) using Chimera, the RFC1 subunit was deleted, and the resulting model including Ctf18, subunits RFC2-5 and PCNA was rigid-body fitted into the cryo-EM map. The model was edited and real-space refined with Coot (57) following flexible fitting performed with ISOLDE (58). A final real-space refinement was performed in Phenix (59), applying secondary structure constraints. The models of both CTF18–PCNA complexes with and without the Mg^{2+} ion were generated similarly.

Acknowledgments

This research was supported by King Abdullah University of Science and Technology (KAUST) through core funding (to S.M.H. and A.D.B.). We thank Lingyun Zhao, Ashraf Al-Alamoudi, Alessandro Genovese and Rachid Sougrat for their assistance at the Imaging and Characterization Core Lab at KAUST.

Author Contributions

S.M.H. and A.D.B conceived and supervised the study. M.T. and A.A. purified the proteins and carried out functional studies. G.R.B. and C.G.S. performed cryo-EM imaging and processing. G.R.B., P.Q-N., and A.D.B. performed model building and validation. G.R.B. and A.D.B. wrote the manuscript with contributions from the other authors.

Data Availability

The maps of CTF18-RFC-ATP-PCNA and CTF18-RFC-ATP-Mg^{2+}-PCNA complexes have been deposited in the EMBD with accession codes EMD-60534, and EMD-60598 and the atomic models in the Protein Data Bank under accession codes PDB 8ZWO and PDB 9IIN.

Ethics declarations

Competing interests

The authors declare no competing interests.

Figures

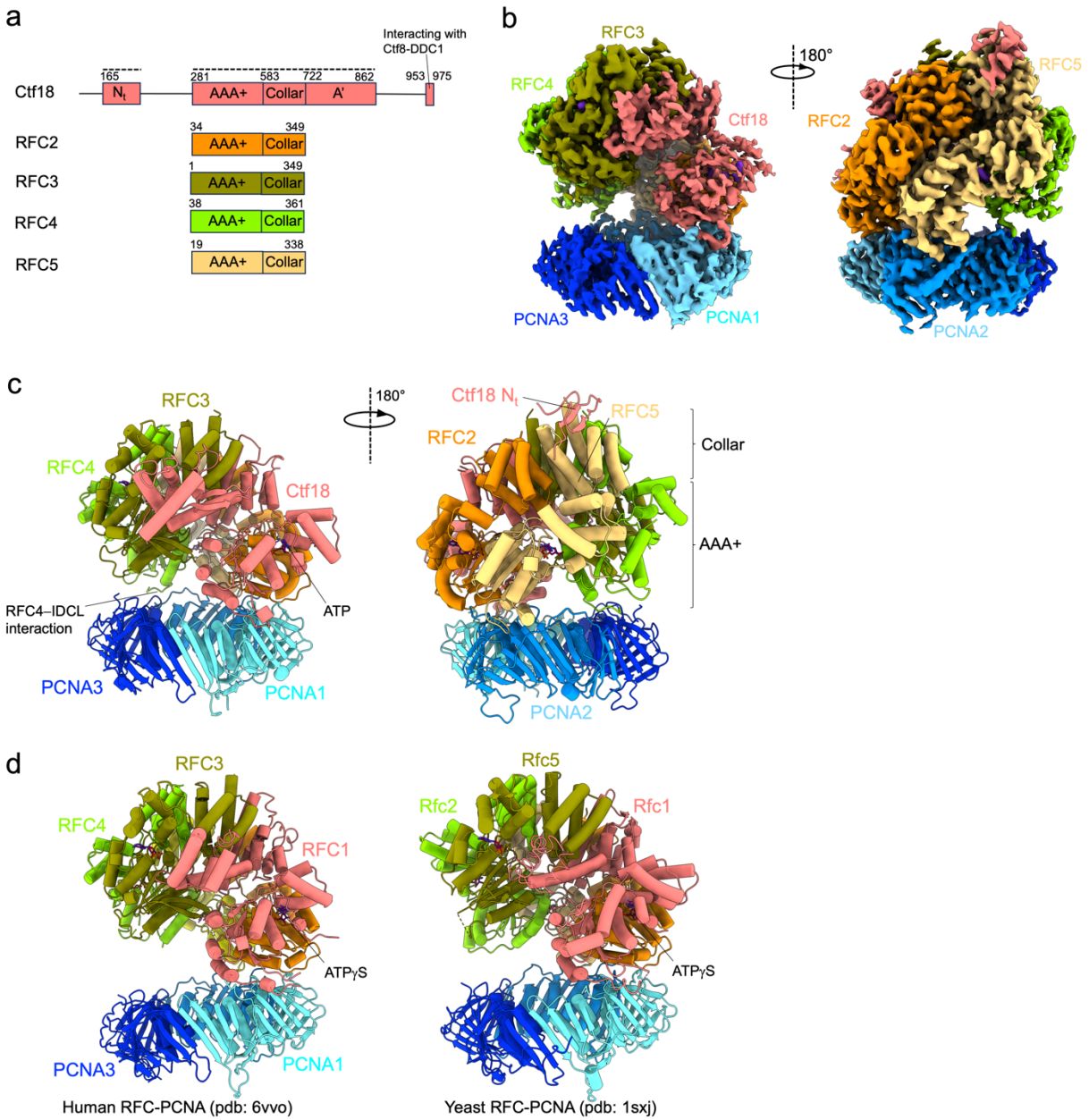

Figure 1. ***Cryo-EM structure of the human CTF18-PCNA complex in the presence of ATP.*** **a)** Domain organization of the CTF18 subunits forming the RFC pentamer. The dotted line above the Ctf18 subunit highlights the regions that are observed in the cryo-EM map. **b)** Two views of the cryo-EM map of the CTF18–PCNA complex, colored by subunits. The less sharp definition of the map region corresponding to the AAA+ domain of the Ctf18 subunit supports a relatively high mobility of this subunit. **c)** Molecular

model of the CTF18–PCNA complex in ribbon representation. **d)** Structures of the human (left) (10) and *Saccharomyces cerevisiae* (right) RFC–PCNA complex (8), which present the RFC pentamer in an auto-inhibited conformation analogous to the one captured in the CTF18–PCNA complex.

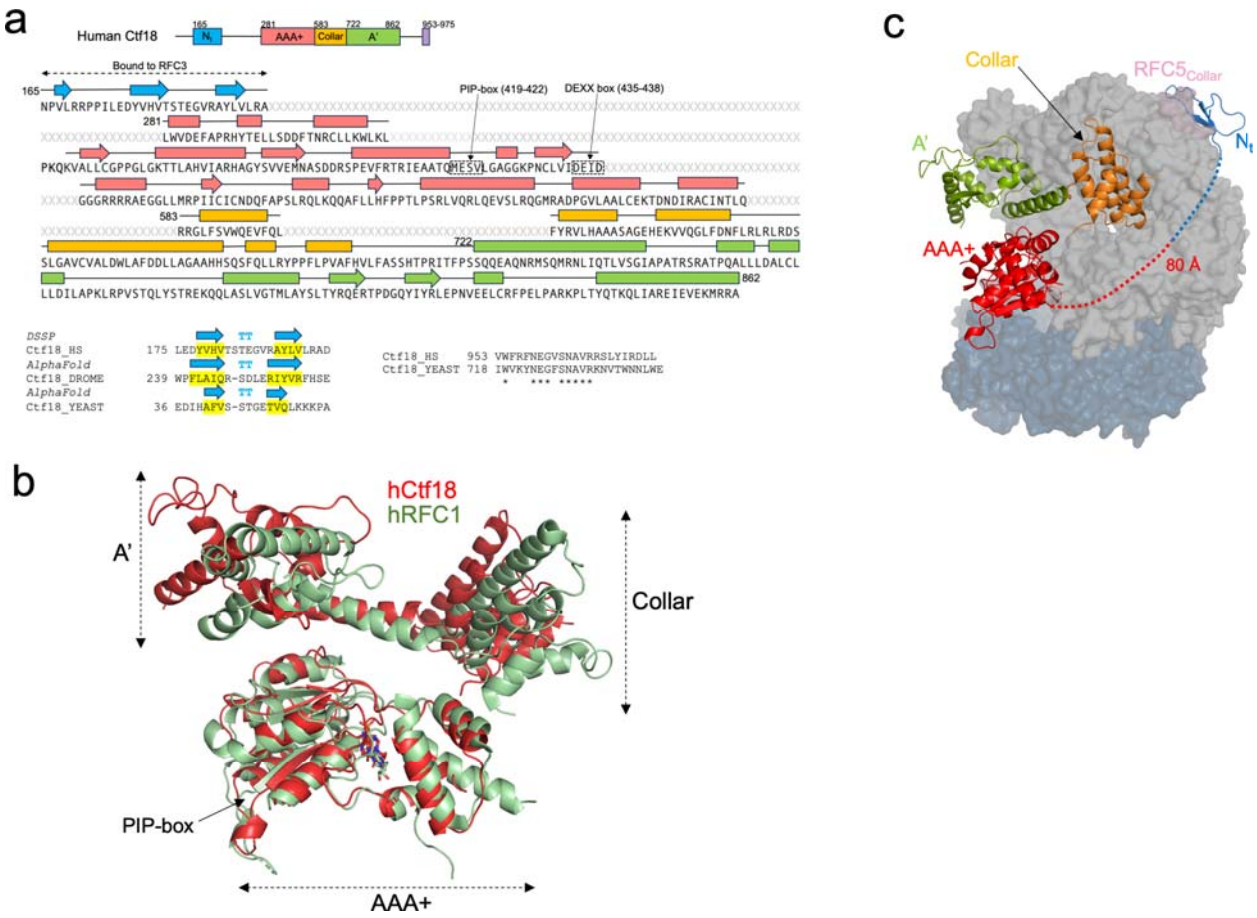

Figure 2. ***Structure of the Ctf18 subunit.*** **a)** Sequence of the human Ctf18 subunit, highlighting the secondary structural elements as assigned in the cryo-EM model. The atypical PCNA-interacting motif (PIP-box) and conserved DEXX box are boxed. Below the Ctf18 sequence to the left, the sequences of the N-terminus of human and other lower eukaryotes Ctf18, together with the secondary prediction by AlphaFold (42) are

shown, highlighting the conservation of the β-hairpin fold. Below the Ctf18 sequence to the right, the alignment of the C-terminal region of human and *Saccharomyces cerevisiae* Ctf18, which interacts with the Ctf8/Dcc1 subunits, is shown. Asterisks denote conserved residues. **b)** Superposition of the human Ctf18 and RFC1 (PDB: 6VVO (10)) subunit structures, with subdomains labeled. **c)** Structure of the Ctf18 subunit, in ribbon representation, within the CTF18–PCNA complex. The Ctf18 subdomains are colored-coded as in panel **(a)**. The other complex subunits are shown as surfaces

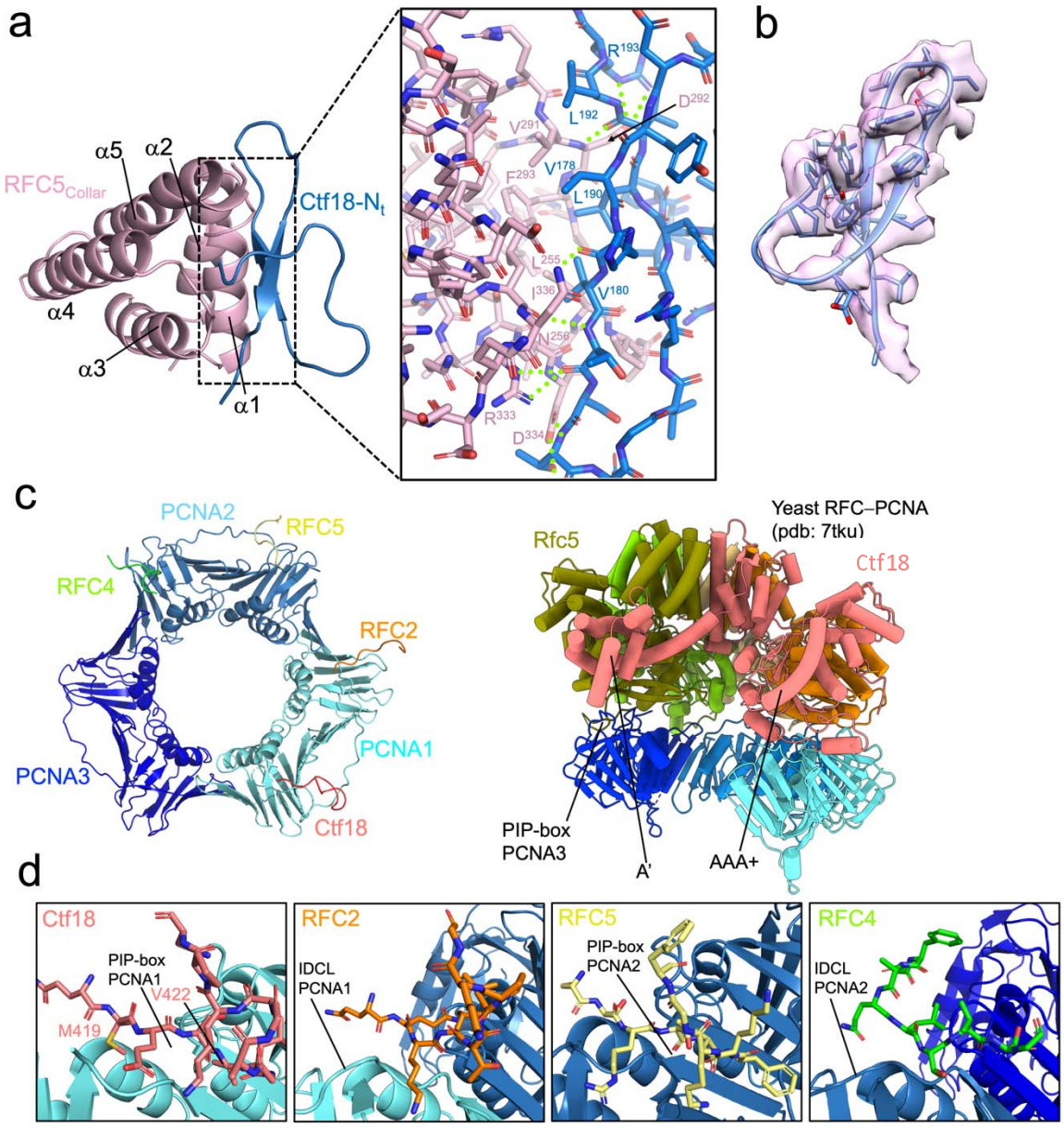

Figure 3. ***Structural details of the Ctf18-RFC5 and CTF18-PCNA interactions.*** **a)** Model of the RFC5 collar domain and Ctf18 N-terminal β-hairpin in ribbon representation. The inset shows the interface in stick representation, with hydrogen bonds shown as green dotted lines. **b)** Map region around the Ctf18 N-terminal β-hairpin. **c)** Model of the PCNA homotrimer bound to the four CTF18 interacting regions. To the right, the structure of the yeast RFC–PCNA complex (11) with an open clamp,

highlighting the engagement of all five RFC subunits to PCNA, required for clamp opening. **d)** Model of the regions of the CTF18–PCNA interactions, with CTF18 subunit residues shown as sticks and PCNA as ribbon.

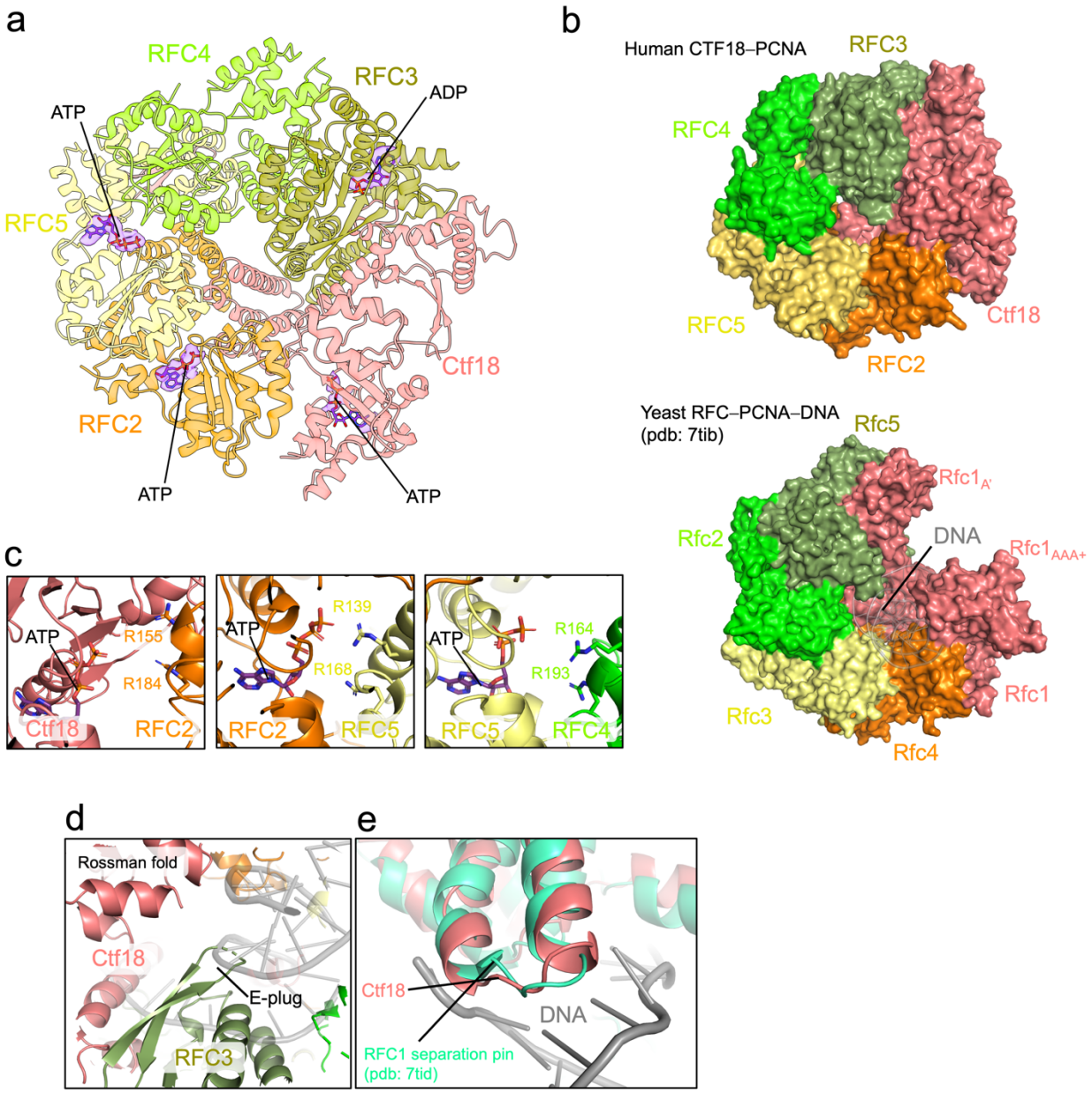

Figure 4. ***Analysis of the auto-inhibited conformation of the CTF18 pentamer and nucleotide coordination*. a)** Ribbon model of the CTF18 pentamer (PCNA hidden).

Nucleotide molecules are shown as sticks, with the corresponding cryo-EM density. **b)** Surface representation of (top) the CTF18 pentamer and (bottom) the yeast RFC pentamer bound to open PCNA and primer-template DNA (11). PCNA is hidden in both structures. The overtwisted CTF18 pentamer cannot accommodate DNA within the inner chamber. **c)** Model of the ATP active sites in the CTF18–PCNA complex, showing disruption of the interactions mediated by the arginine fingers. **d)** Detail of the inner chamber region of the CTF18 pentamer, showing the β-hairpin (E-plug) of RFC5 protruding in the region predicted to be occupied by DNA. The DNA (grey ribbon) is modeled as in the yeast RFC–DNA–PCNA complex (11). **e)** The structures of the RFC1 subunit of the RFC–DNA–PCNA complex (11) and the Ctf18 subunit of the CTF18–PCNA complex are aligned to highlight the conservation of the separation pin interacting with DNA.

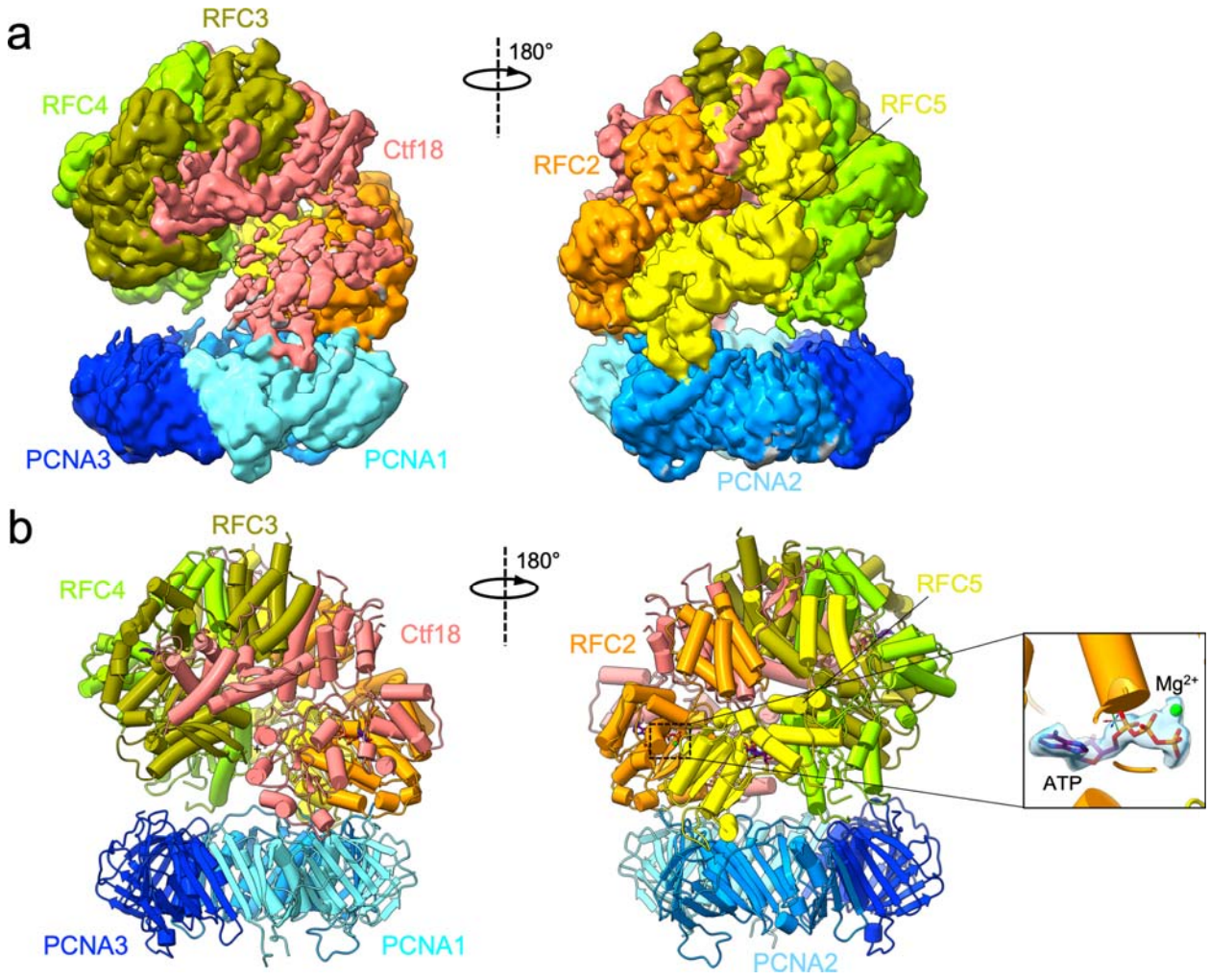

Figure 5. ***Cryo-EM structure of the human CTF18-PCNA complex in the presence of ATP and Mg^{2+}.*** **a)** Two views of the Cryo-EM map, colored by subunits. **b)** Molecular model in ribbon representation. The inset shows a map and model of the ATP molecule bound to the RFC2 subunit, with a discernible Mg^{2+} ion.

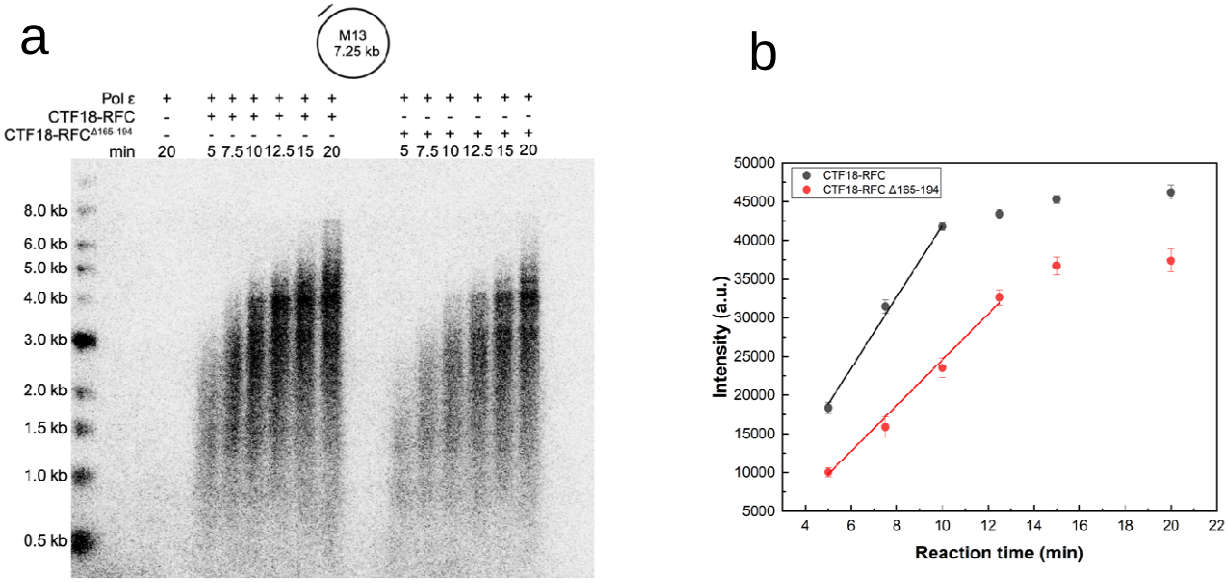

Figure 6. ***Primer extension assay with Pol ε and CTF18-RFC WT or CTF18-RFC$^{\Delta 165-194}$.*** **a)** Time course reactions on M13mp18 single-strand DNA with 40 nM CTF18-RFC or CTF18-RFC$^{\Delta 165-194}$. Reactions were performed as described in Materials and Methods. **b)** Quantification of the band intensities from the primer extension assay shows that the rate of increase in intensity, derived from the initial linear portion of the reaction time before saturation, is 4142 ± 95 a.u./min for CTF18-RFC and 2389 ± 143 a.u./min for CTF18-RFC$^{\Delta 165-194}$. This indicates that the mutant slows Pol ε synthesis by 42%. The experiment was conducted three times. Dots in **b)** represent mean values from the three replicas.

a

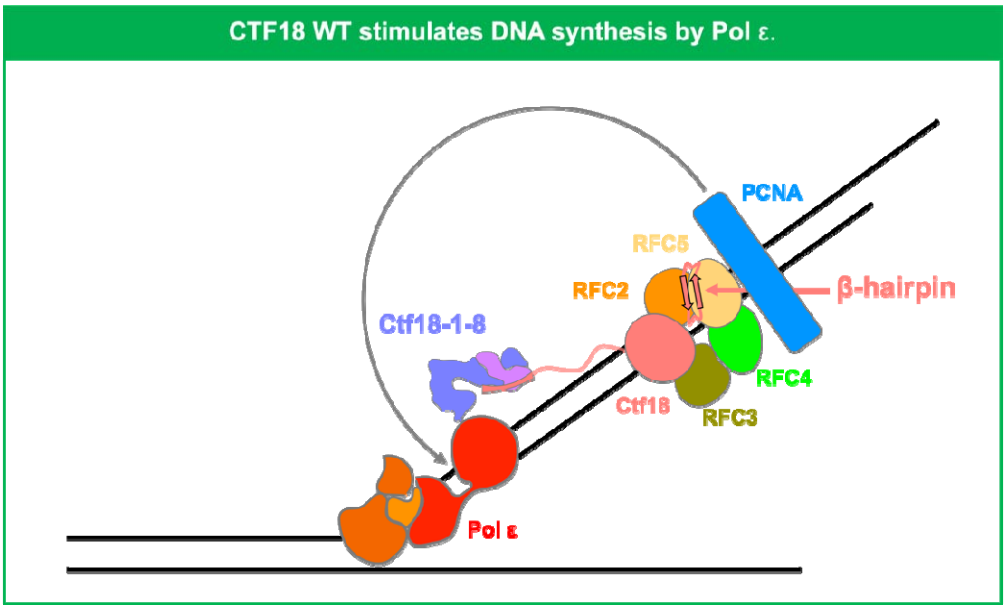

b

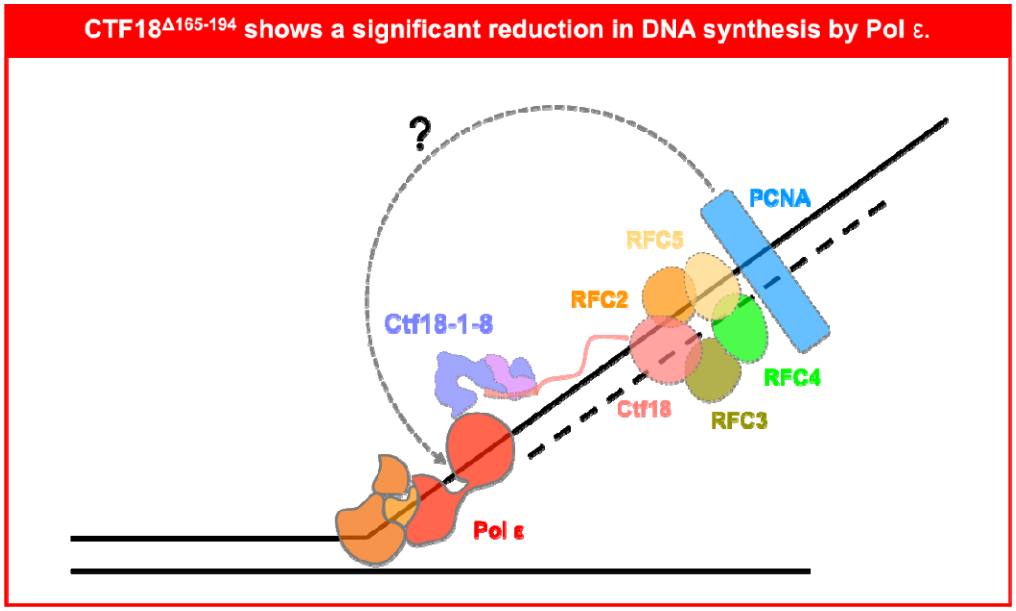

Figure 7. ***Deletion of the N-terminal β-hairpin of the CTF18 large subunit reduces DNA synthesis by Pol ε.*** **a)** The structure of the RFC module of CTF18 is stabilized by the presence of a β-hairpin in the Ctf18 subunit (amino acids 165-194). Thus, wild type CTF18 stimulates DNA synthesis by Pol ε interacting with the polymerase and recruiting

the sliding clamp PCNA. **b)** The stability of the CTF18–PCNA complex is compromised by the deletion of the β-hairpin. Consequently, a CTF18 deletion mutant lacking the β-hairpin (CTF18$^{\Delta 165\text{-}194}$) shows lower activity in stimulating Pol ε primer synthesis.

References

1. Hubscher U, Maga G, Spadari S. Eukaryotic DNA polymerases. Annu Rev Biochem. 2002;71:133-63.
2. Choe KN, Moldovan GL. Forging Ahead through Darkness: PCNA, Still the Principal Conductor at the Replication Fork. Mol Cell. 2017;65(3):380-92.
3. Moldovan GL, Pfander B, Jentsch S. PCNA controls establishment of sister chromatid cohesion during S phase. Mol Cell. 2006;23(5):723-32.
4. Indiani C, O'Donnell M. The replication clamp-loading machine at work in the three domains of life. Nat Rev Mol Cell Biol. 2006;7(10):751-61.
5. Kelch BA, Makino DL, O'Donnell M, Kuriyan J. Clamp loader ATPases and the evolution of DNA replication machinery. BMC Biol. 2012;10:34.
6. Kang MS, Ryu E, Lee SW, Park J, Ha NY, Ra JS, et al. Regulation of PCNA cycling on replicating DNA by RFC and RFC-like complexes. Nat Commun. 2019;10(1):2420.
7. Jeruzalmi D, O'Donnell M, Kuriyan J. Crystal structure of the processivity clamp loader gamma (gamma) complex of E. coli DNA polymerase III. Cell. 2001;106(4):429-41.
8. Bowman GD, O'Donnell M, Kuriyan J. Structural analysis of a eukaryotic sliding DNA clamp-clamp loader complex. Nature. 2004;429(6993):724-30.
9. Kazmirski SL, Podobnik M, Weitze TF, O'Donnell M, Kuriyan J. Structural analysis of the inactive state of the Escherichia coli DNA polymerase clamp-loader complex. Proc Natl Acad Sci U S A. 2004;101(48):16750-5.
10. Gaubitz C, Liu X, Magrino J, Stone NP, Landeck J, Hedglin M, et al. Structure of the human clamp loader reveals an autoinhibited conformation of a substrate-bound AAA+ switch. Proc Natl Acad Sci U S A. 2020;117(38):23571-80.
11. Gaubitz C, Liu X, Pajak J, Stone NP, Hayes JA, Demo G, et al. Cryo-EM structures reveal high-resolution mechanism of a DNA polymerase sliding clamp loader. Elife. 2022;11.
12. Schrecker M, Castaneda JC, Devbhandari S, Kumar C, Remus D, Hite RK. Multistep loading of a DNA sliding clamp onto DNA by replication factor C. Elife. 2022;11.
13. Turner J, Hingorani MM, Kelman Z, O'Donnell M. The internal workings of a DNA polymerase clamp-loading machine. EMBO J. 1999;18(3):771-83.
14. Gomes XV, Schmidt SL, Burgers PM. ATP utilization by yeast replication factor C. II. Multiple stepwise ATP binding events are required to load proliferating cell nuclear antigen onto primed DNA. J Biol Chem. 2001;276(37):34776-83.
15. Chen S, Levin MK, Sakato M, Zhou Y, Hingorani MM. Mechanism of ATP-driven PCNA clamp loading by S. cerevisiae RFC. J Mol Biol. 2009;388(3):431-42.
16. Simonetta KR, Kazmirski SL, Goedken ER, Cantor AJ, Kelch BA, McNally R, et al. The mechanism of ATP-dependent primer-template recognition by a clamp loader complex. Cell. 2009;137(4):659-71.
17. Kelch BA, Makino DL, O'Donnell M, Kuriyan J. How a DNA polymerase clamp loader opens a sliding clamp. Science. 2011;334(6063):1675-80.
18. Kelch BA. Review: The lord of the rings: Structure and mechanism of the sliding clamp loader. Biopolymers. 2016;105(8):532-46.

19. Jeruzalmi D, O'Donnell M, Kuriyan J. Clamp loaders and sliding clamps. Curr Opin Struct Biol. 2002;12(2):217-24.
20. Lee KY, Park SH. Eukaryotic clamp loaders and unloaders in the maintenance of genome stability. Exp Mol Med. 2020;52(12):1948-58.
21. Mayer ML, Gygi SP, Aebersold R, Hieter P. Identification of RFC(Ctf18p, Ctf8p, Dcc1p): an alternative RFC complex required for sister chromatid cohesion in S. cerevisiae. Mol Cell. 2001;7(5):959-70.
22. Naiki T, Kondo T, Nakada D, Matsumoto K, Sugimoto K. Chl12 (Ctf18) forms a novel replication factor C-related complex and functions redundantly with Rad24 in the DNA replication checkpoint pathway. Mol Cell Biol. 2001;21(17):5838-45.
23. Bylund GO, Burgers PM. Replication protein A-directed unloading of PCNA by the Ctf18 cohesion establishment complex. Mol Cell Biol. 2005;25(13):5445-55.
24. Crabbe L, Thomas A, Pantesco V, De Vos J, Pasero P, Lengronne A. Analysis of replication profiles reveals key role of RFC-Ctf18 in yeast replication stress response. Nat Struct Mol Biol. 2010;17(11):1391-7.
25. Liu HW, Bouchoux C, Panarotto M, Kakui Y, Patel H, Uhlmann F. Division of Labor between PCNA Loaders in DNA Replication and Sister Chromatid Cohesion Establishment. Mol Cell. 2020;78(4):725-38 e4.
26. al-Khodairy F, Carr AM. DNA repair mutants defining G2 checkpoint pathways in Schizosaccharomyces pombe. EMBO J. 1992;11(4):1343-50.
27. Kim J, Robertson K, Mylonas KJ, Gray FC, Charapitsa I, MacNeill SA. Contrasting effects of Elg1-RFC and Ctf18-RFC inactivation in the absence of fully functional RFC in fission yeast. Nucleic Acids Res. 2005;33(13):4078-89.
28. Bermudez VP, Lindsey-Boltz LA, Cesare AJ, Maniwa Y, Griffith JD, Hurwitz J, et al. Loading of the human 9-1-1 checkpoint complex onto DNA by the checkpoint clamp loader hRad17-replication factor C complex in vitro. Proc Natl Acad Sci U S A. 2003;100(4):1633-8.
29. Terret ME, Sherwood R, Rahman S, Qin J, Jallepalli PV. Cohesin acetylation speeds the replication fork. Nature. 2009;462(7270):231-4.
30. Zhang J, Shi X, Li Y, Kim BJ, Jia J, Huang Z, et al. Acetylation of Smc3 by Eco1 is required for S phase sister chromatid cohesion in both human and yeast. Mol Cell. 2008;31(1):143-51.
31. Rolef Ben-Shahar T, Heeger S, Lehane C, East P, Flynn H, Skehel M, et al. Eco1-dependent cohesin acetylation during establishment of sister chromatid cohesion. Science. 2008;321(5888):563-6.
32. Unal E, Heidinger-Pauli JM, Kim W, Guacci V, Onn I, Gygi SP, et al. A molecular determinant for the establishment of sister chromatid cohesion. Science. 2008;321(5888):566-9.
33. Kubota T, Nishimura K, Kanemaki MT, Donaldson AD. The Elg1 replication factor C-like complex functions in PCNA unloading during DNA replication. Mol Cell. 2013;50(2):273-80.
34. Stokes K, Winczura A, Song B, Piccoli G, Grabarczyk DB. Ctf18-RFC and DNA Pol form a stable leading strand polymerase/clamp loader complex required for normal and perturbed DNA replication. Nucleic Acids Res. 2020;48(14):8128-45.
35. Bermudez VP, Maniwa Y, Tappin I, Ozato K, Yokomori K, Hurwitz J. The alternative Ctf18-Dcc1-Ctf8-replication factor C complex required for sister chromatid cohesion loads proliferating cell nuclear antigen onto DNA. Proc Natl Acad Sci U S A. 2003;100(18):10237-42.

36. Fujisawa R, Ohashi E, Hirota K, Tsurimoto T. Human CTF18-RFC clamp-loader complexed with non-synthesising DNA polymerase epsilon efficiently loads the PCNA sliding clamp. Nucleic Acids Res. 2017;45(8):4550-63.
37. Grabarczyk DB, Silkenat S, Kisker C. Structural Basis for the Recruitment of Ctf18-RFC to the Replisome. Structure. 2018;26(1):137-44 e3.
38. Jones ML, Baris Y, Taylor MRG, Yeeles JTP. Structure of a human replisome shows the organisation and interactions of a DNA replication machine. EMBO J. 2021;40(23):e108819.
39. Langston LD, Zhang D, Yurieva O, Georgescu RE, Finkelstein J, Yao NY, et al. CMG helicase and DNA polymerase epsilon form a functional 15-subunit holoenzyme for eukaryotic leading-strand DNA replication. Proc Natl Acad Sci U S A. 2014;111(43):15390-5.
40. Yeeles JTP, Janska A, Early A, Diffley JFX. How the Eukaryotic Replisome Achieves Rapid and Efficient DNA Replication. Mol Cell. 2017;65(1):105-16.
41. Chilkova O, Stenlund P, Isoz I, Stith CM, Grabowski P, Lundstrom EB, et al. The eukaryotic leading and lagging strand DNA polymerases are loaded onto primer-ends via separate mechanisms but have comparable processivity in the presence of PCNA. Nucleic Acids Res. 2007;35(19):6588-97.
42. Jumper J, Evans R, Pritzel A, Green T, Figurnov M, Ronneberger O, et al. Highly accurate protein structure prediction with AlphaFold. Nature. 2021;596(7873):583-9.
43. Cai J, Uhlmann F, Gibbs E, Flores-Rozas H, Lee CG, Phillips B, et al. Reconstitution of human replication factor C from its five subunits in baculovirus-infected insect cells. Proc Natl Acad Sci U S A. 1996;93(23):12896-901.
44. Podust VN, Tiwari N, Ott R, Fanning E. Functional interactions among the subunits of replication factor C potentiate and modulate its ATPase activity. J Biol Chem. 1998;273(21):12935-42.
45. Cai J, Yao N, Gibbs E, Finkelstein J, Phillips B, O'Donnell M, et al. ATP hydrolysis catalyzed by human replication factor C requires participation of multiple subunits. Proc Natl Acad Sci U S A. 1998;95(20):11607-12.
46. Schmidt SL, Gomes XV, Burgers PM. ATP utilization by yeast replication factor C. III. The ATP-binding domains of Rfc2, Rfc3, and Rfc4 are essential for DNA recognition and clamp loading. J Biol Chem. 2001;276(37):34784-91.
47. Seybert A, Wigley DB. Distinct roles for ATP binding and hydrolysis at individual subunits of an archaeal clamp loader. EMBO J. 2004;23(6):1360-71.
48. Sakato M, O'Donnell M, Hingorani MM. A central swivel point in the RFC clamp loader controls PCNA opening and loading on DNA. J Mol Biol. 2012;416(2):163-75.
49. Liu J, Zhou Y, Hingorani MM. Linchpin DNA-binding residues serve as go/no-go controls in the replication factor C-catalyzed clamp-loading mechanism. J Biol Chem. 2017;292(38):15892-906.
50. He Q, Wang F, O'Donnell M, Huilin L. Cryo-EM reveals a nearly complete PCNA loading process and unique features of the human alternative clamp loader CTF18-RFC. PNAS. 2024; 121(18).
51. Yuan Z, Georgescu R, Yao NY, Yurieva O, O'Donnell ME, Li H. Mechanism of PCNA loading by Ctf18-RFC for leading-strand DNA synthesis. Science. 2024;385.

52. Zheng SQ, Palovcak E, Armache JP, Verba KA, Cheng Y, Agard DA. MotionCor2: anisotropic correction of beam-induced motion for improved cryo-electron microscopy. Nat Methods. 2017;14(4):331-2.
53. Rohou A, Grigorieff N. CTFFIND4: Fast and accurate defocus estimation from electron micrographs. J Struct Biol. 2015;192(2):216-21.
54. Kimanius D, Dong L, Sharov G, Nakane T, Scheres SHW. New tools for automated cryo-EM single-particle analysis in RELION-4.0. Biochem J. 2021;478(24):4169-85.
55. Bepler T, Morin A, Rapp M, Brasch J, Shapiro L, Noble AJ, et al. Positive-unlabeled convolutional neural networks for particle picking in cryo-electron micrographs. Nat Methods. 2019;16(11):1153-60.
56. Kelley LA, Mezulis S, Yates CM, Wass MN, Sternberg MJ. The Phyre2 web portal for protein modeling, prediction and analysis. Nat Protoc. 2015;10(6):845-58.
57. Emsley P, Lohkamp B, Scott WG, Cowtan K. Features and development of Coot. Acta Crystallogr D Biol Crystallogr. 2010;66(Pt 4):486-501.
58. Croll TI. ISOLDE: a physically realistic environment for model building into low-resolution electron-density maps. Acta Crystallogr D Struct Biol. 2018;74(Pt 6):519-30.
59. Adams PD, Afonine PV, Bunkoczi G, Chen VB, Davis IW, Echols N, et al. PHENIX: a comprehensive Python-based system for macromolecular structure solution. Acta Crystallogr D Biol Crystallogr. 2010;66(Pt 2):213-21.

Supplementary Information
Structure of the human CTF18 clamp loader bound to PCNA

Briola G. R. *et al*

Includes:

Supplementary Figures 1-9

Supplementary Table 1

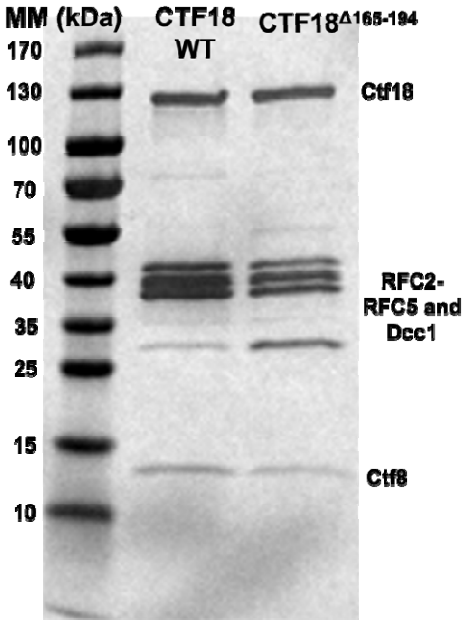

S1 Fig. *SDS-PAGE gel (4-20%) of the purified human clamp loader CTF18 WT and CTF18$^{\Delta 165\text{-}194}$*. Bands corresponding to the different subunits are labeled. The molecular weight standard is shown.

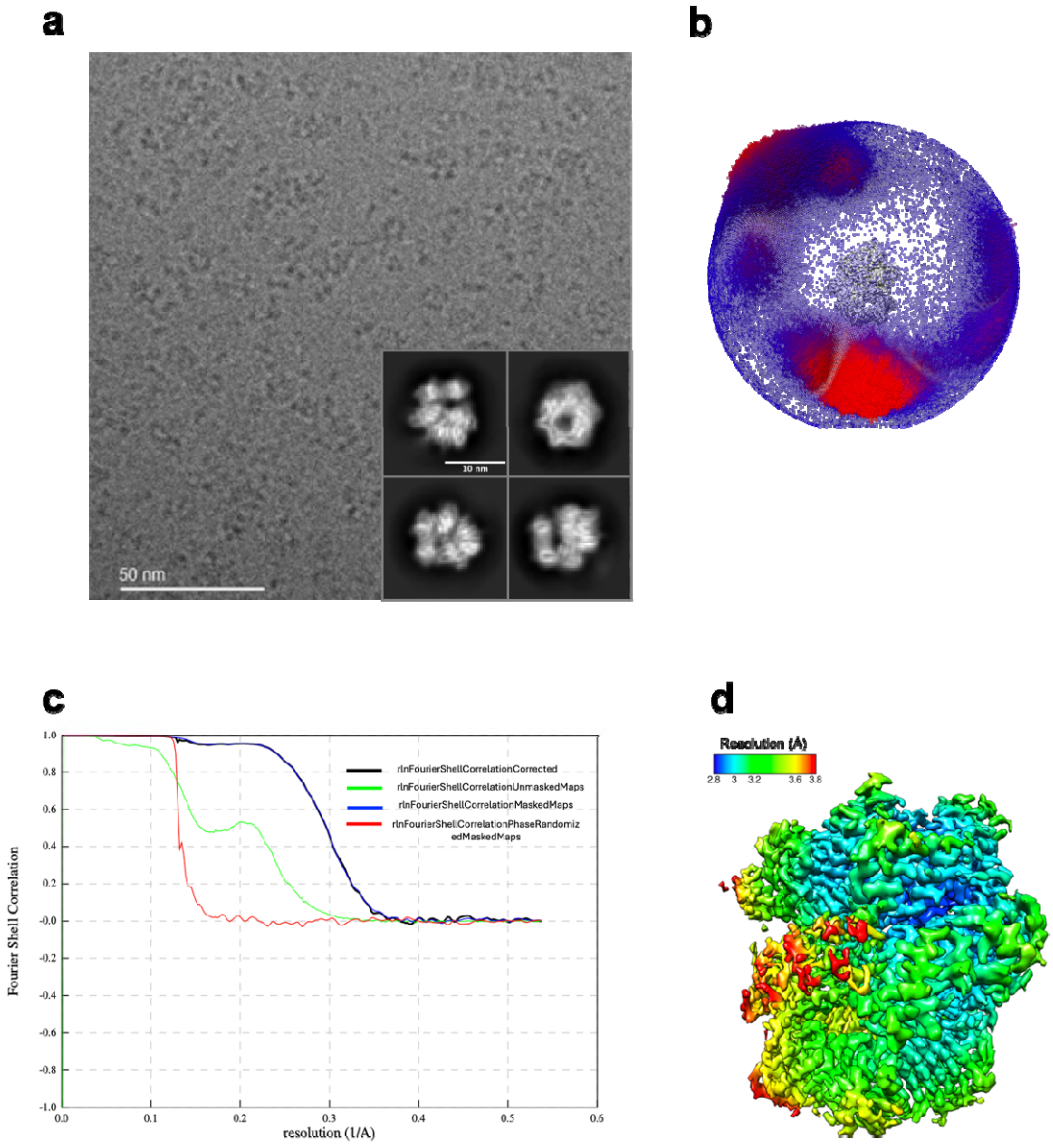

S2 Fig. *Cryo-EM of the CTF18–PCNA complex in the presence of ATP.* **a)** Representative electron micrograph acquired on a Falcon 4i electron detector in counting mode, and representative 2D class averages. **b)** Angular distributions of projections. **c)** Gold-standard Fourier shell correlation for the reconstruction of the full complex after postprocessing, and resolution estimation using the 0.143 criterion. **d)** Cryo-EM map of the complex, color-coded by local resolution.

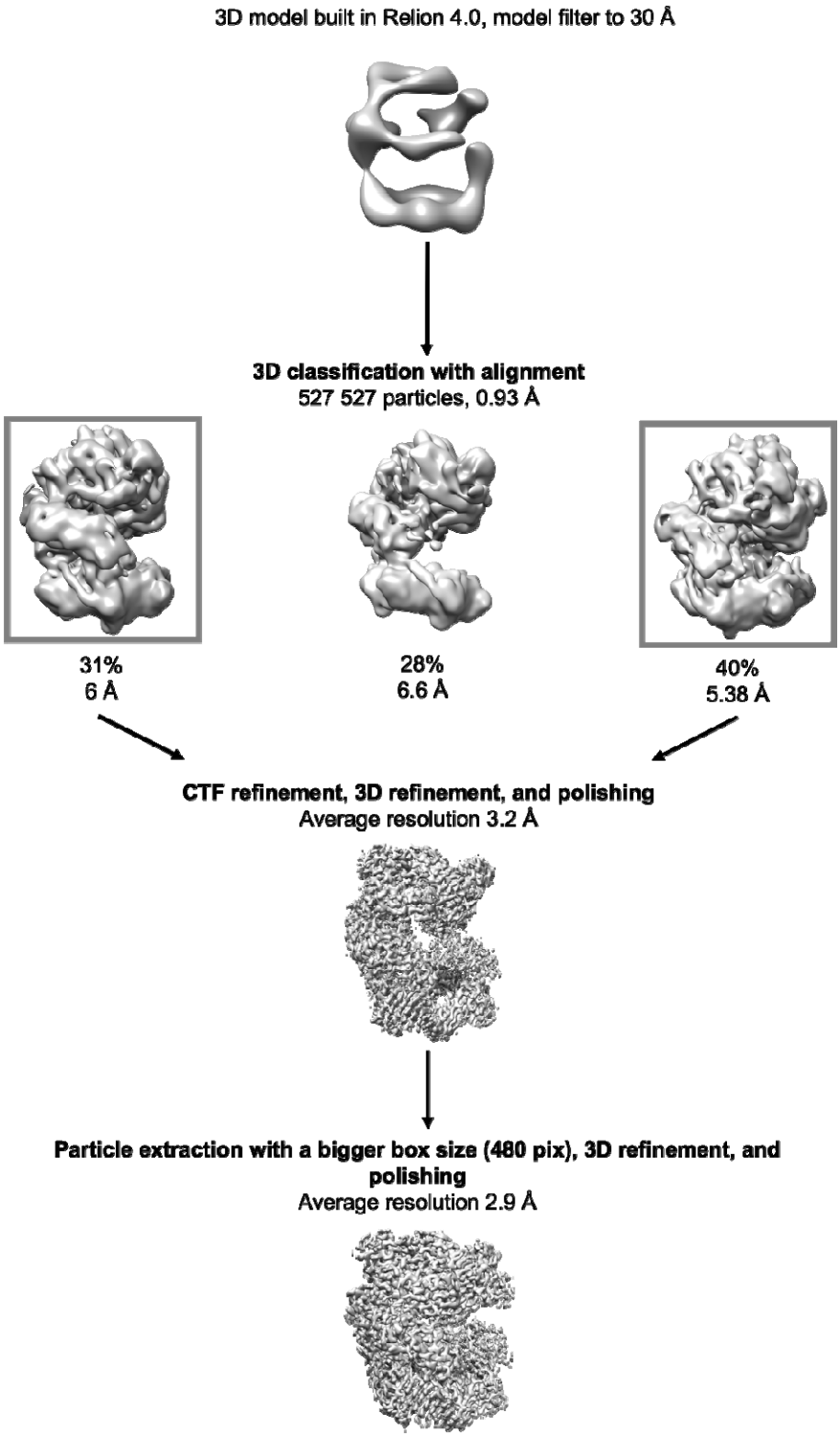

S3 Fig. Workflow of cryo-EM image processing and 3D reconstruction of CTF18-RFC-PCNA complex in the presence of 0.5 mM ATP and without Mg^{2+} **(Dataset 1)**. Relion 4.0 was used for image processing and 3D reconstruction.

a

Walker A sequence
Consensus: GxxGxGK T/S

```
Ctf18:      374- GPPGLGKT -381
hRFC1:      651- GPPGVGKT -658
```

b

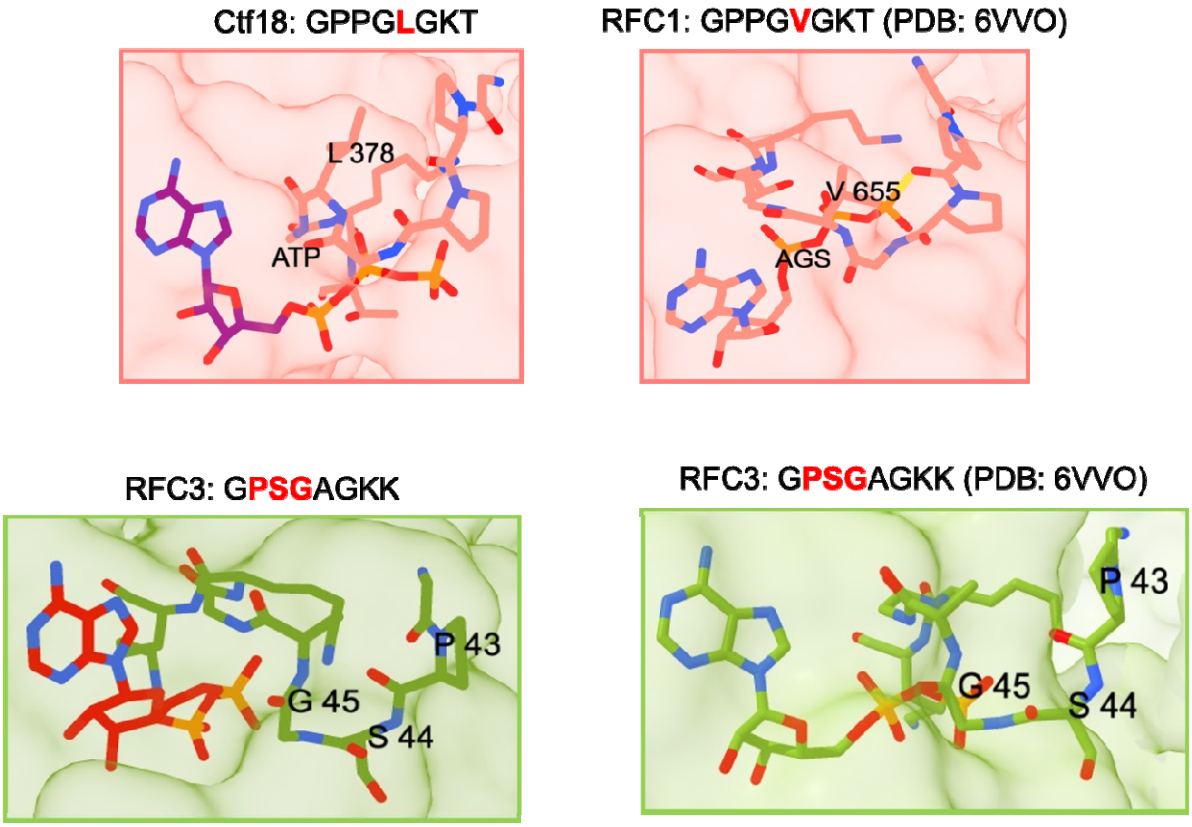

S4 Fig. *Walker A sequence and structure.* **a)** Walker A sequence comparison between CTF18 and hRFC (PDB: 6VVO). **b)** The upper panels illustrate the conformation of the Walker A motifs in Ctf18 and RFC1 (PDB: 6VVO). The lysine residue instead of valine does not seem to alter the loop conformation. The lower panels show the Walker A motif in the RFC3 subunit of CTF18 in the current study (left) and of hRFC (PDB: 6VVO) (right). Alterations in the motif appear to block ATP binding (10). S44 replaces the canonical proline, possibly preventing ATP binding.

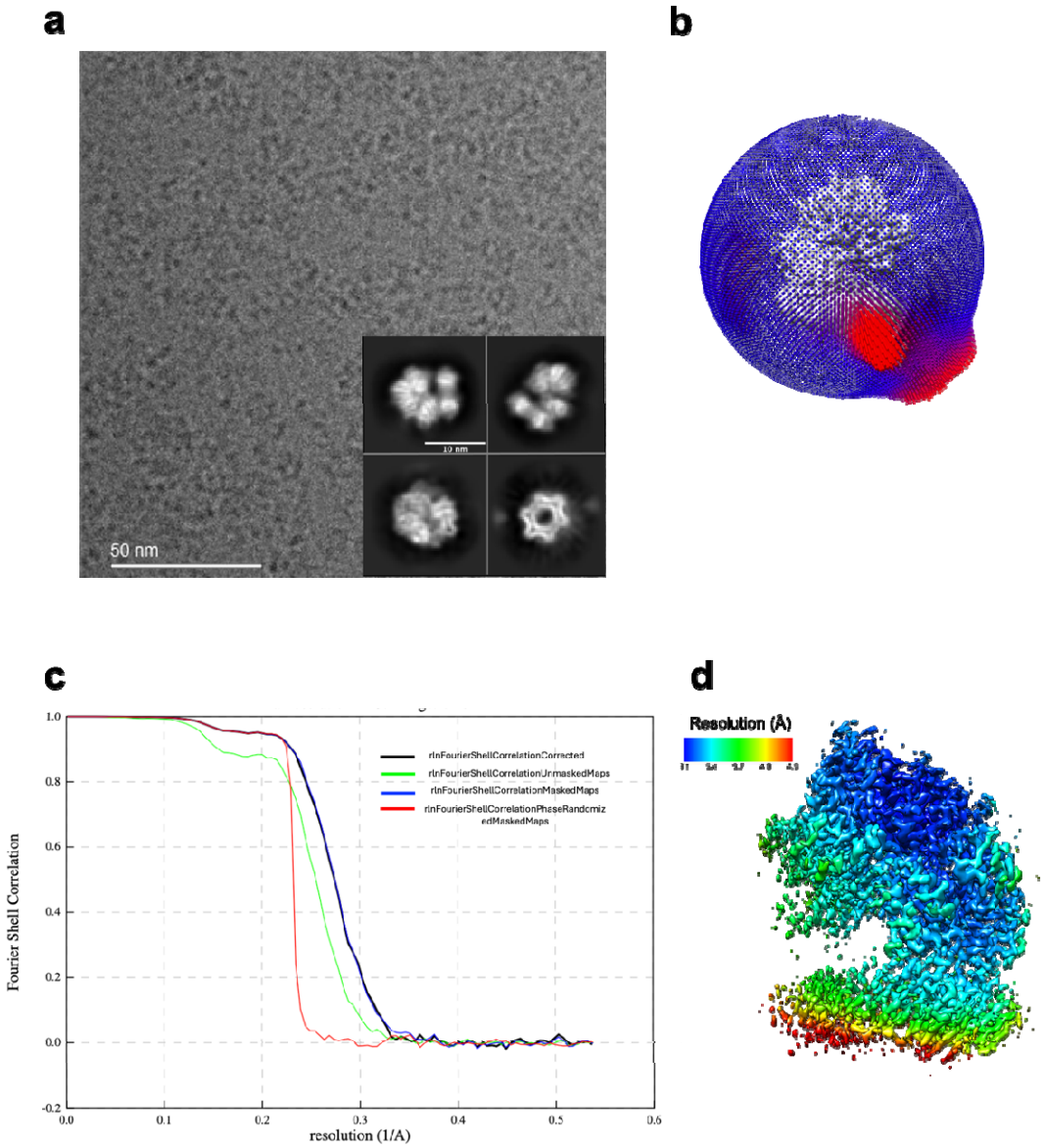

S5 Fig. *Cryo-EM of the CTF18–PCNA complex in the presence of ATP and Mg^{2+}.* **a)** Representative electron micrograph acquired on a Falcon 4i electron detector in counting mode, and representative 2D class averages. **b)** Angular distributions of projections. **c)** Gold-standard Fourier shell correlation for the reconstruction of the full complex after focused refinement, and resolution estimation using the 0.143 criterion. **d)** Cryo-EM map of the complex, color-coded by local resolution.

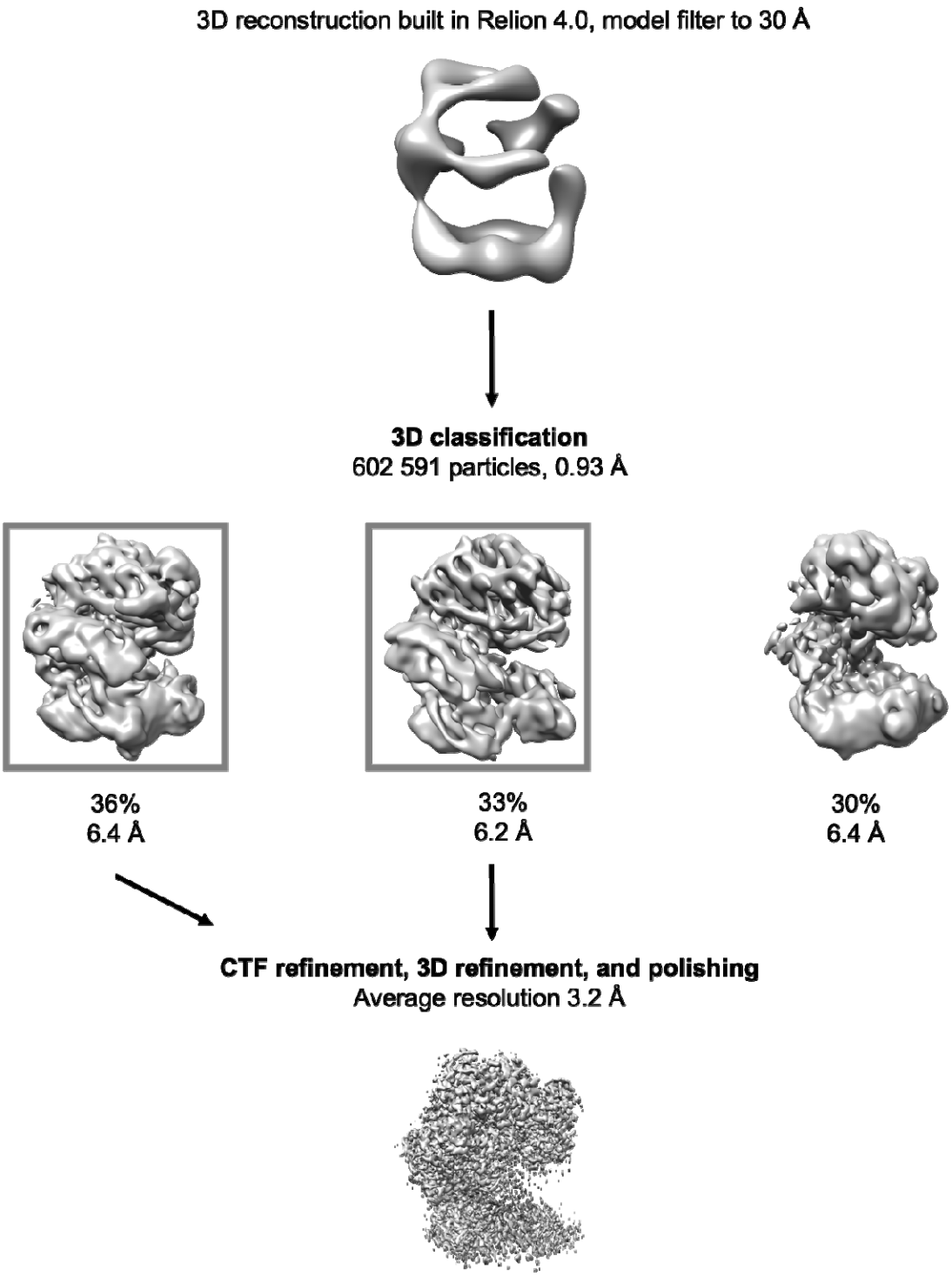

S6 Fig. Workflow of cryo-EM image processing and 3D reconstruction of CTF18-RFC-PCNA complex in the presence of 0.5 mM ATP and 5 mM Mg^{2+} **(Dataset 2)**. Relion 4.0 was used for image processing and 3D reconstruction.

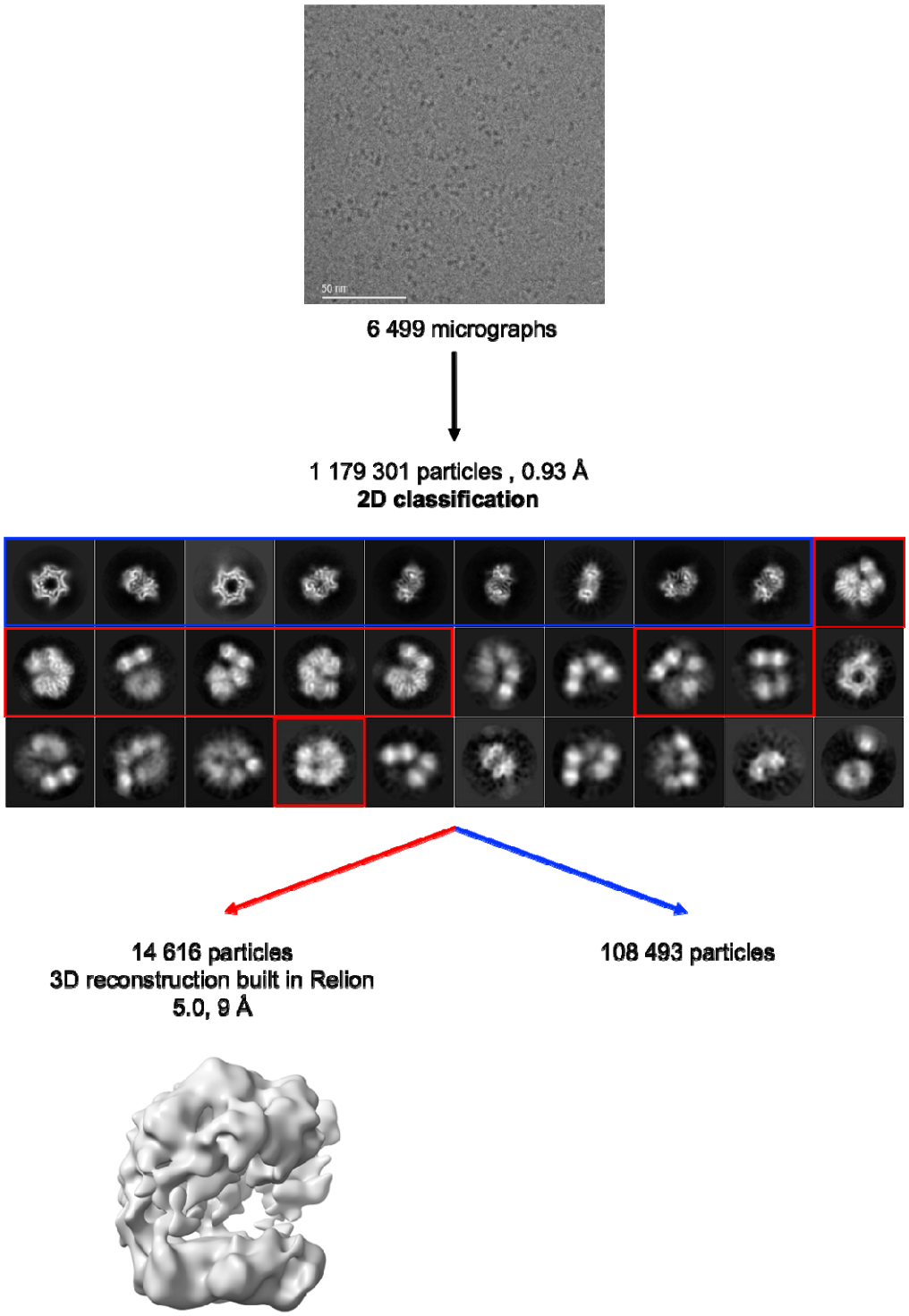

S7 Fig. Workflow of cryo-EM image processing and 3D reconstruction of *CTF18-RFC*$^{\Delta 165\text{-}194}$-PCNA complex in the presence of 0.5 mM ATP and without Mg^{2+} **(Dataset 3)**. Relion 5.0 was used for image processing and 3D reconstruction.

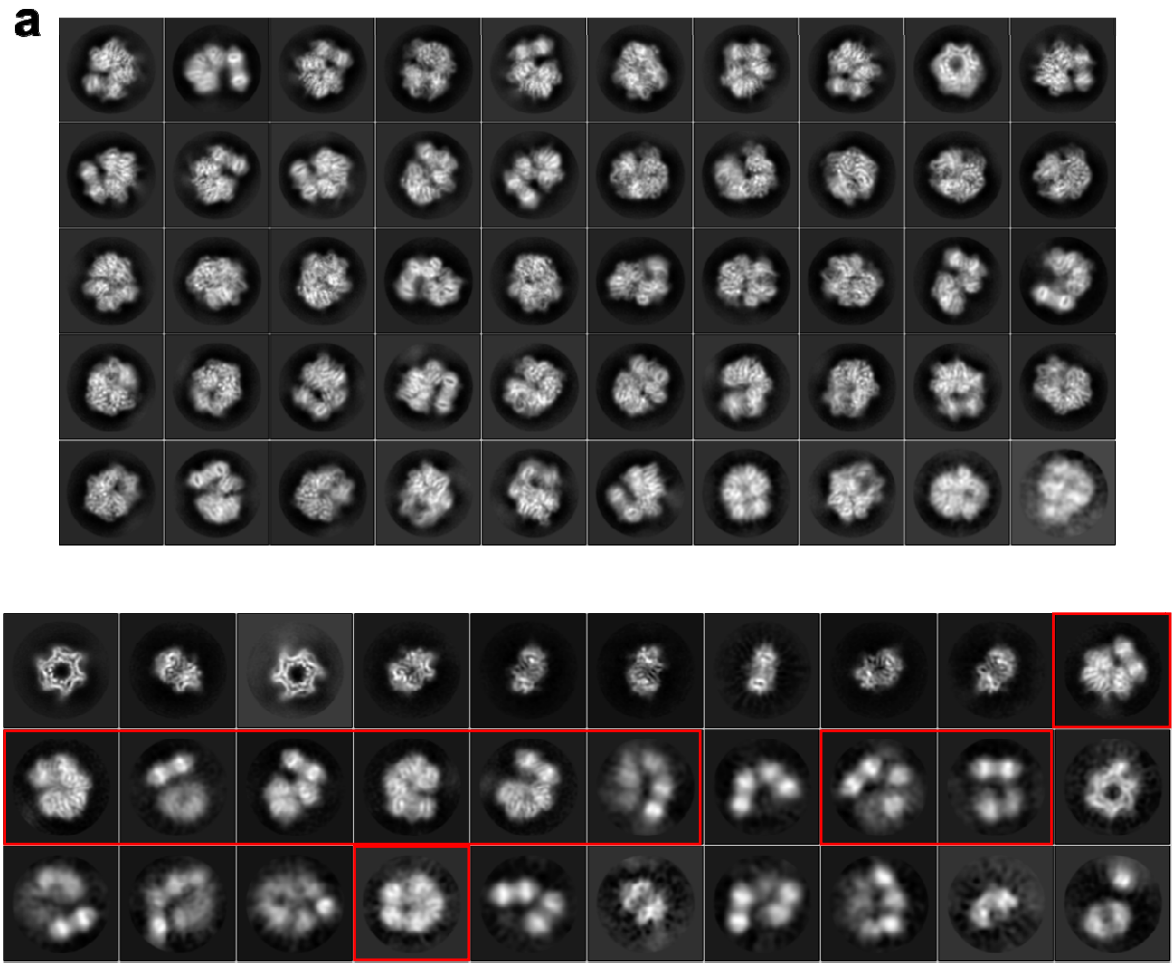

S8 Fig. *2D classification of CTF18 WT and CTF18-RFC$^{\Delta 165\text{-}194}$.* **a)** The 2D classification of CTF18-RFC WT reveals the formation of the CTF18-RFC-PCNA complex with clear structural integrity (515 195 particles in all the showed 2D classes) **b)** The 2D classification of CTF18-RFC$^{\Delta 165\text{-}194}$ mutant highlights the impact of β-hairpin deletion on complex stability. The presence of different orientations of the PCNA ring alone indicates that the absence of the β-hairpin contributes to the increased instability of the complex. Only the 2D classes squared in red represent the CTF18-RFC$^{\Delta 165\text{-}194}$ -PCNA complex (14 616 particles).

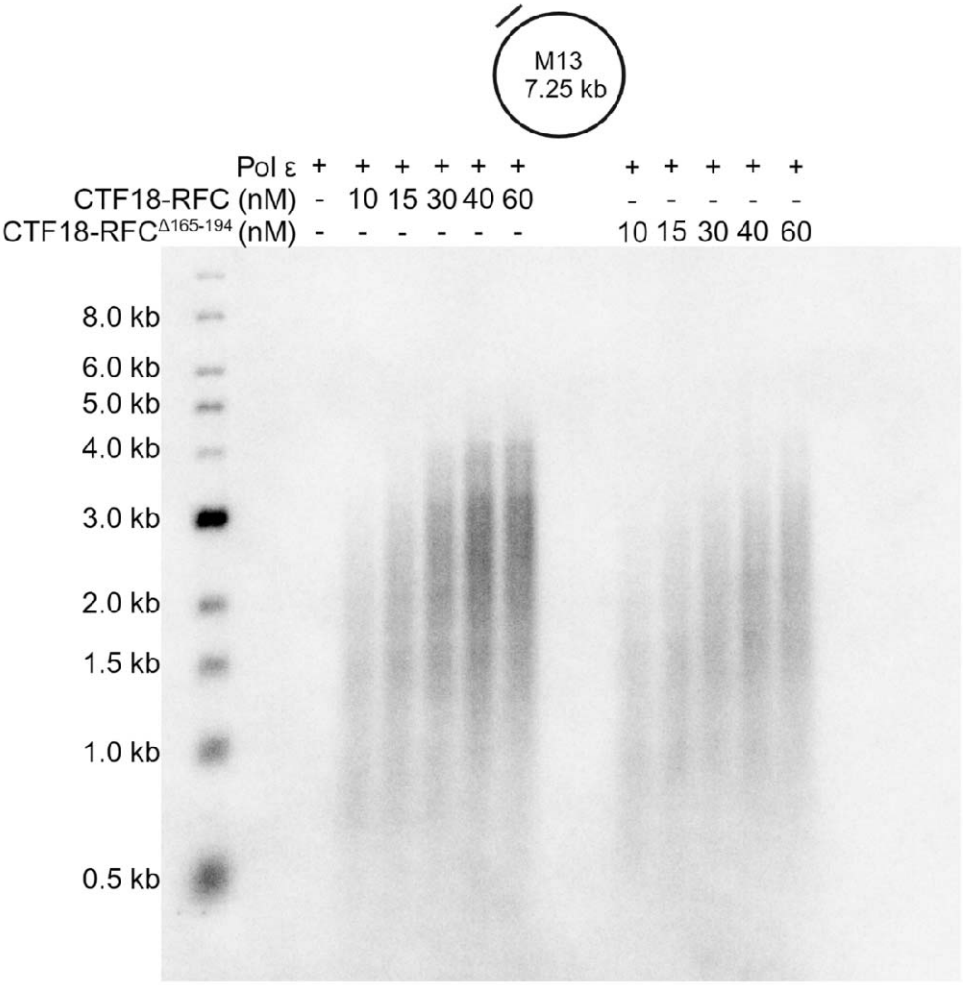

S9 Fig. *Primer extension assays with Pol ε and CTF18 WT and CTF18-RFC$^{\Delta 165\text{-}194}$.* CTF18-RFC or *CTF18-RFC$^{\Delta 165\text{-}194}$* concentration titration reactions on M13mp18 single-strand DNA. Reactions were running for 10 mins at 37°C.

	CTF18-PCNA with ATP	CTF18-PCNA with ATP and Mg^{2+}
Data collection and processing		
Magnification	130,000	130,000
Voltage (kV)	300	300
Electron exposure (e–/Å^2)	43	46
Defocus range (μm)	-2.7 to -1.5	-2.7 to -1.5
Pixel size (Å)	0.93	0.93
Symmetry imposed	C1	C1
Initial particle images (no.)	2,043,120	3,216,167
Final particle images (no.)	527,527	602,591
Map resolution (Å)	2.9	3.3
FSC threshold	0.143	0.143
Map resolution range (Å)	2.8-3.8	3.1-4.3
Refinement		
Initial model used (PDB code)	6VVO	6VVO
Model resolution (Å)	3.0	3.5
FSC threshold	0.5	0.5
Map sharpening *B* factor (Å^2)	-67.879	-138.637
Model composition		
Non-hydrogen atoms	19777	19779
Protein residues	2503	2503
Ligands	4	6
B factors (Å^2)		
Protein	68.48	169.79
Ligand	80.11	167.64
R.m.s. deviations		
Bond lengths (Å)	0.004	0.003
Bond angles (°)	0.612	0.547
Validation		
MolProbity score	2.26	2.00
Clashscore	11.75	9.39
Poor rotamers (%)	3.47	2.19
Ramachandran plot		
Favored (%)	96.14	96.38
Allowed (%)	3.82	3.49
Disallowed (%)	0.04	0.12

S1 Table. Cryo-EM data collection, model refinement, and validation statistics.